*Article*

# Effect of MWCNTs Functionalization on Thermal, Electrical, and Ammonia-Sensing Properties of MWCNTs/PMMA and PHB/MWCNTs/PMMA Thin Films Nanocomposites

Raina Aman Qazi [1,2,*], Rozina Khattak [2,*], Luqman Ali Shah [1], Rizwan Ullah [1], Muhammad Sufaid Khan [3], Muhammad Sadiq [4], Mahmoud M. Hessien [5] and Zeinhom M. El-Bahy [6]

1   National Centre of Excellence in Physical Chemistry, Polymer Laboratory, University of Peshawar, Peshawar 25120, Pakistan; luqman_alisha@yahoo.com (L.A.S.); drrizwan@uop.edu.pk (R.U.)
2   Department of Chemistry, Shaheed Benazir Bhutto Women University, Peshawar 25000, Pakistan
3   Department of Chemistry, University of Malakand, Chakdara 18800, Pakistan; sufaidkhan1984@uom.edu.pk
4   Department of Chemistry, Quaid-i-Azam University, Islamabad 45320, Pakistan; m_sidiq12@yahoo.com
5   Department of Chemistry, College of Science, Taif University, P.O. Box 11099, Taif 21944, Saudi Arabia; m.hessien@tu.edu.sa
6   Department of Chemistry, Faculty of Science, Al-Azhar University, Nasr City, Cairo 11884, Egypt; zeinelbahy@azhar.edu.eg
*   Correspondence: rainaaman@sbbwu.edu.pk (R.A.Q.); rznkhattak@sbbwu.edu.pk (R.K.)

**Abstract:** Partially biodegradable polymer nanocomposites Poly(3-Hydroxybutyrate) (PHB)/MultiwalledCarbon Nanotubes (MWCNTs)/Poly(Methyl Methacrylate) (PMMA)and non-biodegradable nanocomposites (MWCNTs/PMMA) were synthesized, and their thermal, electrical, and ammonia-sensing properties were compared. MWCNTs were chemically modified to ensure effective dispersion in the polymeric matrix. Pristine MWCNTs (p-MWCNTs) were functionalized with –COOH (a-MWCNTs) and amine groups (f-MWCNTs). Then, PHB grafted multiwalled carbon nanotubes (g-MWNTs) were prepared by a 'grafting to' technique. The p-MWCNTs, a-MWCNTs, f-MWCNTs, and g-MWCNTs were incorporated into the PMMA matrix and PMMA/PHB blend system by solution mixing. The PHB/f-MWCNTs/PMMA blend system showed good thermal properties among all synthesized nanocomposites. Results from TGA and dTGA analysis for PHB/f-MWCNTs/PMMA showed delay in $T_5$ (about 127 °C), $T_{50}$ (up to 126 °C), and $T_{max}$ (up to 65 °C) as compared to neat PMMA. Higher values of frequency capacitance were observed in nanocomposites containing f-MWCNTs and g-MWCNTs as compared to nanocomposites containing p-MWCNTs and a-MWCNTs. This may be attributed to their excellent interaction and good dispersion in the polymeric blend. Analysis of ammonia gas-sensing data showed that PHB/g-MWCNTs/PMMA nanocomposites exhibited good sensitivity (≈100%) and excellent repeatability with a constant response. The calculated limit of detection (LOD) is 0.129 ppm for PHB/g-MWCNTs/PMMA, while that of all other nanocomposites is above 40 ppm.

**Keywords:** nanocomposites; multiwalled carbon nanotubes; poly(3-hydroxybutyrate); poly(methyl methacrylate); ammonia sensors; thermal stability; electrical properties

## 1. Introduction

Polymers are versatile materials that have certain unique properties such as lowdensity, flexibility, toughness, easy processibility, and low conductivity [1]. However, these properties are still inadequate for efficient industrial applications. Hence, continuous research efforts are in progress to develop new polymeric materials with advanced properties. The desired properties can be obtained by adding filler (organic and inorganic materials) to the polymer matrix. Common fillers such as metal particles, silica, carbon black, etc. require high filler loading. High filler loading increases the costof composites along with challenging processibility. Nowadays, nanofillers are incorporated in polymer matrixes to

introduce desired properties with low filler loading [1]. Nanofillers (size range: 1–100 nm) offer a range of excellent and adjustable physical and chemical properties [2]. One of the most extensively studied and used nanomaterials are carbon nanotubes (CNT). Extraordinary chemical and physical properties of the CNT (i.e. high stability, good conductivity, wide availability and easy functionalization) offer several advantages as compared to other commonly used materials [3,4]. CNTs are much sought after due to their nanoscale size, which confers exceptional thermal, electrical, mechanical, optical, and chemical capabilities [5].Conducting polymer nanocomposite is formed when the dispersed filler link through CNTs junctions within polymeric matrix. The creation of percolated pathways leads to the conduction of electrons and phonons. As a result, the composite transformed from an insulator to conductor [6]. Uniformly distributed CNTs in the polymeric matrix lowers the percolation threshold [7,8].

CNTs have been proved to be a potential gas sensing material for tiny, portable, and low-sensing devices in the preceding decade [9]. Their small size and high surface area provide a large number of sites for the adsorption of gas molecule, as well as their good electrical sensitivity, room temperature operation, and stability, making them a strong candidate for technological sensors [10]. Toxic gas sensing with semiconducting carbon nanotubes (as chemical and biological sensors) has been proposed [11]. Literature review shows that CNTs revealed good sensitivity to gases such as $H_2$, $NH_3$, $NO_2$, $SO_2$, CO, $CH_4$, $O_2$ and $H_2S$. The adsorption of substrate molecules on the sidewalls of CNTs alters its electrical properties [12]. This change in electrical properties can be utilized as output signals in CNTs based sensors [13]. The major mechanism of sensing at the low temperature is electrical charge transfer among the gas molecules and MWCNTs [14]. Gases such as $NH_3$, $NO_2$, etc. adsorb directly on the surface of CNTs and cause the transfer of electrons, which changes the electrical conductivity of the nanotubes. To ameliorate the sensitivity characteristics of resistive gas sensors, the addition of polymers to carbon nanotubes is practiced widely these days. The van der Walls attraction between CNTs results in agglomerations [15,16]. Such agglomeration reduces the number of adsorption sites and the resulting gas sensors depict less sensitivity. The interfacial bonding between CNTs and the polymer is poor [17]. Agglomeration also disrupts percolation routes and degrades mechanical characteristics, resulting in a subpar composite [18–20]. The interaction of carbon nanotubes with the polymer matrix is required for synergistic effects [21]. This is favored by the chemical modification of MWCNTs with functional groups such as COOH, OH, and $NH_3$. The newly introduced functional groups are capable of interaction with functional groups of the polymer matrix. These interactions can either be physical or chemical. Thus, the composites exhibit good interfacial adhesion and improved dispersion of modified MWCNTs in the polymeric matrix. Chemical functionalization can introduce desirable properties with respect to the amount and type of organic moieties deposited on the surface of CNTs [22]. Moreover, functionalized CNTs showed improved sensitivity and selectivity of the gas sensor [9].

In the last few years, biodegradable polymers obtained from renewable resources have gained significant consideration as a possible substitute for non-compostable polymers [23] which causes several environmental issues. In this study, poly(3-hydroxybutyrate) (PHB) has been selected, as a biodegradable polymer. PHB is water-insoluble and shows resistance to hydrolytic degradation [24]. These characteristics set PHB apart from the most currently used biodegradable polymers, which are either water-soluble or moisture sensitive. PHB is also biocompatible, non-toxic, and UV resistant, as well as having a high tensile strength (40 Mpa). These characteristics make PHB the best choice for a biodegradable sensor [25]. PHB is a delicate and rigid substance. When maintained at room temperature for an extended period of time, it becomes brittle. PHB's brittleness and thermal instability make it difficult to use in a variety of applications [26]. The large crystal size of PHB carries poor mechanical properties [27]. Due to poor mechanical properties, limited functionalities, high manufacturing cost, thermal degradability just above the melting point, PHB needs modifications for enhanced performance in particular applications [28]. Frequent efforts

were made to mix PHB with other flexible polymers or low atomic weight plasticizers to transform PHB into materials with enhanced mechanical strength and film formation [29,30]. Various researchers attempted to blend PHB with other polymers to attain the physical characteristics, and to reduce the fragility of PHB. Properties of PHB can be improved by blending it with Poly(methyl methacrylate) (PMMA). PMMA is a non-biodegradable thermoplastic. It is suitable for application in electrical engineering because of its good dielectric constant and low humidity/water absorption capability. Heat stabilized types can resist temperature up to 100 °C and show good resistance to temperature change [31]. PMMA has been selected due to its advantages such as low cost, easy molding and easy processing [32]. Abou [33] and Yong et. al. [34] indicated that a-PHB/PMMA blend shows improved miscibility when the content of PMMA is greater than 60 wt%.

Studies showed that the incorporation of functionalized MWCNTs even in a small amount can significantly improve the thermal, mechanical and electrical characteristics of PHB [35,36]. However, just a few studies on the preparation, characterization and properties of PHB based polymer nanocomposites have been reported. The bionanocomposites created by the uniform distribution of carbon-based nanofillers in a biopolymer matrix have a lot of potential [37–39]. The effect of MWCNTs functionalization on the thermal, electrical and ammonia-sensing capabilities of MWCNTs(4 wt%)/PMMA and PHB/MWCNTs (4 wt%)/PMMA thin films nanocomposites systems was investigated in this study.

## 2. Materials and Methods

### 2.1. Materials

MWCNTs (diameter: 80–100 nm), sulfuric acid ($H_2SO_4$ 98%), hydrochloric acid (HCl 37%), nitric acid (65%), chloroform (99.8%), ethanol (99.7%), tetrahydrofuran (THF), N.N-dimethylformamide (DMF) and 4,4'-diaminodiphenyl sulfone (DDS) (MW) $\approx$ 248.3 $gmol^{-1}$) were purchased from Sigma Aldrich. PMMA (99.8% pure, average molecular weight (MW) $\approx$ 10,000 $gmol^{-1}$) and PHB (98% pure, average molecular weight (MW) $\approx$ 760,000 $gmol^{-1}$) were provided by BDH chemicals Ltd Poole, England.

### 2.2. Functionalization of MWCNTs

p-MWCNTs and 3:1 solution of $H_2SO_4$ (8 M) and $HNO_3$ (5 M) were refluxed at 60 °C for 5 h to introduce carboxylic group on the surface of MWCNTs. Acid functionalized MWCNTs (a-MWCNTs) thus obtained were filtered with a microfiltration membrane (0.4 μm). To attain neutral pH, the obtained a-MWCNTs were subsequently washed with distilled water [40]. The fabrication of amine-functionalized MWCNTs was performed by following a method developed by Freitas et al. [41] with slight modification. One g of the a-MWCNTs were treated with 10 g of DDS solution in *N*,*N*-dimethylformamide. The solution was refluxed at 65 °C for 98 h. The amine-functionalized MWCNTs (f-MWCNTs) that, formed were washed with THF after microfiltration to remove residual DDS and then were then dried for 7 h in a vacuum oven at 70 °C. For the synthesis of grafted or block polymeric structures with amphiphilic or biodegradable characteristics, a method developed by Yu et al [42] with slight modification was followed. The PHB and f-MWCNTs in a 1:2 ratio were refluxed in chloroform for 95 h at 62 °C. The g-MWCNTs obtained were filtered through a microfiltration membrane (0.4 μm) and were in a vacuum dried environment at 78 °C for 7 h.

### 2.3. Fabrication of Multiwalled Carbon Nanotubes (MWCNTs)/Polymethylmethacrylate (PMMA) Nanocomposite

The p-MWCNTs/PMMA, a-MWCNTs/PMMA, f-MWNTs/PMMA, andg-MWCNTs/ PMMA nanocomposite were fabricated by solution casting method. First, 0.5 wt%, 1 wt%, 2 wt%, 4 wt%, 5 wt% and 10 wt% of each type of MWCNTs were added separately in 4 mL chloroform and sonicated for 2 h in separate conical flasks. In separate conical flasks, PMMA (2 g) in chloroform (6 mL) was stirred for 2 h. Then, the different weight fraction of each type of MWCNTs was added to PMMA and refluxed (at 60 °C for 96 h). After stirring,

the samples were solution cast in clean and dry Petri dishes. The synthesized samples were vacuum dried in an oven until their weight was equilibrated and were then kept in a desiccator for minimal humidity effects.

### 2.4. Fabrication of Poly(3-Hydroxybutyrate) (PHB)/Multiwalled Carbon Nanotubes (MWCNTs)/ Poly(Methyl Methacrylate) (PMMA)

The solubility limit of PHB with PMMA is 20% by weight. Excess PHB segregates and crystallizes [43], therefore, a different weight fraction of each type of MWCNTs was added in fixed composition of PMMA (80%) and PHB (20%) blend. A similar process was followed for the fabrication of PHB/p-MWCNTs/PMMA, PHB/a-MWCNTs/PMMA, PHB/f-MWCNTs/PMMA and PHB/g-MWCNTs/PMMA blend systems with 20% of PHB and 80% of PMMA as for MWCNTs/PMMA nanocomposites. However, it was observed that PHB/MWCNTs/PMMA samples containing only 4 wt% MWCNTs are capable of forming thin films. Therefore, all studies were performed on the PHB/MWCNTs/PMMA samples comprising 4 wt% of each type of MWCNTs.

### 2.5. Gas-Sensing Set-Up

The fabricated nanocomposites (0.05 μLdrop) were spin-coated (600 rpm) on inter-digitated electrodes (line width: 210 μm, line space: 190 μm and size: 7 mm × 13.4 mm). The gas-sensing set-up was composed of an airtight jar (3.5 mL), a heating pad and a fan. When the system reached a steady state, it was exposed to different concentrations of ammonia at 25 °C with 60 ± 1% RH, Humidity was measured by using digital hygrometer (ExtechRH101, Shanghai, China). Ammonia evaporated with the help of a fan and heating pad. The resistance response was recorded using an LCR meter (HIOKI 3522-50 LCR HiTESTER, Nagano, Japan).

### 2.6. Material Characterization

FTIR spectra of pristine MWCNTs, functionalized MWCNTs, and thin-film nanocomposites were obtained by using anATR-FTIR (Shimadzu, Japan) within the region of 4000–500 cm$^{-1}$ and with the resolution of 2 cm$^{-1}$. For SEM images, a JSM-6490 (JEOL, Tokyo, Japan) electron microscope was used. Thermal degradation characteristics of all synthesized samples were performed using Parkin-Elmer, TGA-7 instrument (Parkin-Elmer, USA). TGA was performed at a scan rate of 10 °C/min over a temperature range of 25–600 °C. The AC conductance and capacitance values of all the synthesized nanocomposites were measured using Agilent LCR Meter E4980A(Agilent, USA) at room temperature (25 °C) with a voltage amplitude of 1.0 V. AC conductance and capacitance values were measured as a function of frequency. Measurements were made in the frequency range of 25 Hz to 2 MHz.

## 3. Results and Discussion

### 3.1. FTIR Analysis

The FTIR spectra of pristine and functionalized MWCNTs are shown in Figure 1. The FTIR spectrum of pristine MWCNTs (Figure 1a) showed a skeletal vibration of aromatic rings (C=C stretching) at 1615 cm$^{-1}$ and 1582 cm$^{-1}$ which indicated the graphitic structure of MWCNTs [44]. In the spectrum of a-MWCNTs (Figure 1b), a new peak appeared at 1739 cm$^{-1}$ in comparison to the spectrum of p-MWCNTs. This peak is attributed to the –C=O stretch of the -COOH group [45].
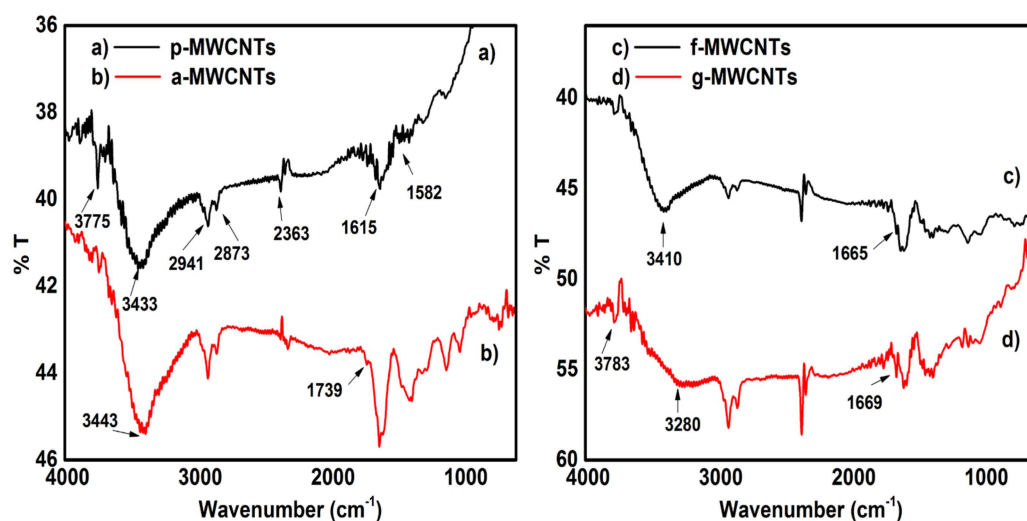
**Figure 1.** FTIR spectra of (**a**) p-MWCNTs, (**b**) a-MWCNTs, (**c**) f-MWCNTs, and (**d**) g-MWCNTs.

In the FTIR spectrum of f-MWCNTs, (Figure 1c) a hump appeared at 1665 cm$^{-1}$, that corresponds to the C=O stretch of the amide structure [40]. A band at 3410 cm$^{-1}$ corresponds to the stretching vibrations of –N-H and –OH [46]. Peaks at 1455 cm$^{-1}$ and 1277 cm$^{-1}$ were attributed to the stretching vibration of C–N in the amide groups. The peaks at 1636 cm$^{-1}$ and 1357 cm$^{-1}$ were assigned to the N-H bending and to the C-N stretching of amine, respectively [47]. A peak at 1636 cm$^{-1}$ shows N-H deformation in primary amines [48]. A peak at 623 cm$^{-1}$ corresponds to the amide structure N-C=O. In the FTIR spectrum of g-MWCNTs (Figure 1d), a peak appeared at 1162 cm$^{-1}$, which corresponds to the C-O-C stretch of grafted PHB. An increase in the peaks intensity at 2920 and 2857 cm$^{-1}$ is due to a large number of the C-H bonds of grafted PHB chains. An increase in the peak intensity at 1669 cm$^{-1}$ (C(=O)NH stretching) and 1552 cm$^{-1}$ (N-H bending) in g-MWCNTs as com-pared to f-MWCNTs shows an increase in the already existing amide bonds due to grafting of PHB polymer on f-MWCNTs [49]. The FTIR spectra and interpretation of MWCNTs(4 wt%)/PMMA and PHB/MWCNTs(4 wt%)/PMMA based nanocomposites have been described in the Supplementary Materials, Text S1 and Figures S1–S3.

*3.2. Morphological Characterization*

SEM image of p-MWCNTs shows the characteristic typical aggregates for MWCNTs structures due to Van der Waals interactions among the tubes (see Supplementary Materials, Figure S4a). However, g-MWCNTs shows entangled thread like structure, which is the characteristic of functionalization (see Supplementary Materials, Figure S4b). Function-alization reduced the aggregates formation. SEM images of fractured surface thin filmed nanocomposites containing p-MWCNTs, a-MWCNTs, f-MWCNTs and g-MWCNTs in the PMMA matrix is shown in Figure 2a–d respectively. Figure 2a showed that p-MWCNTs agglomerated in the PMMA matrix owing to strong van der Waals forces. The smooth-surface of p-MWCNTs exhibits weak interaction with polymer [50]. The nanocomposites comprising of a-MWCNTs and g-MWCNTs [Figure 2b,d] showed no substantial enhance-mentin the morphology. However, in the nanocomposites containing f-MWCNTs, the dispersion has been considerably homogenized. The fractured surfaced SEM image in Figure 2c shows uniformly dispersed tips of untangled f-MWCNTs in PMMA matrix. Amine groups on f-MWCNTs exhibit strong interfacial interaction with PMMA. SEM images of the cryofractured surface of nanocomposites containing p-MWCNTs, a-MWCNTs, f-MWCNTs and g-MWCNTs in PHB/PMMA blend are presented in Figure 2e–h, respectively. The surface morphology changes on the addition of PHB to PMMA/MWCNTs nanocom-posites. Figure 2f–e shows the development of surface morphology from smooth to rough on the addition of PHB to p-MWCNTs(4 wt%)/PMMA and a-MWCNTs(4 wt%)/PMMA nanocomposites. By the addition of f-MWCNTs (4 wt%) [Figure 2g] and g-MWCNTs

(4 wt%) [Figure 2h] in the blend system of PHB/PMMA sponge-like pores appear in the membrane. In Figure 2g,h, the brightest areas show the highest point in the cross-section of the solution cast film and the dark areas indicate the valleys or pores. Thus, it can be inferred that in nanocomposites of PHB/f-MWCNTs(4 wt%)/PMMA and PHB/g-MWCNTs(4 wt%)/PMMA, the PHB/PMMA may wrap around f-MWCNTs and g-MWCNTs, respectively to prevent their aggregation and it is hard to see these nanotubes with in the micrographs.
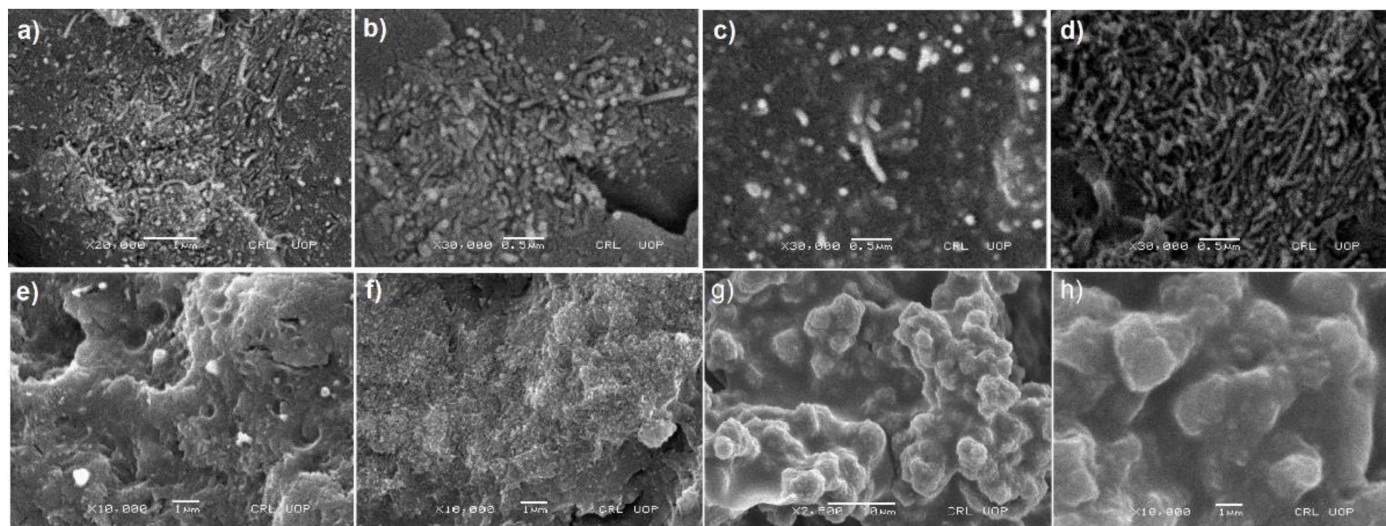


**Figure 2.** SEM images of (**a**) p-MWCNTs(4 wt%)/PMMA, (**b**) a-MWCNTs(4 wt%)/PMMA, (**c**) f-MWCNTs(4 wt%)/PMMA, (**d**) g-MWCNTs(4 wt%)/PMMA (**e**) PMMA/p-MWCNTs(4 wt%)/PHB, (**f**) PMMA/a-MWCNTs(4 wt%)/PHB, (**g**) PMMA/f-MWCNTs(4 wt%)/PHB and, (**h**) PMMA/g-MWCNTs(4 wt%)/PHB.

### 3.3. Electrical Properties

AC electrical conductance for p-MWCNTs/PMMA, a-MWCNTs/PMMA, f-MWCNTs/PMMA, g-MWCNTs/PMMA, and neat PMMA as a function of frequency for different weight fractions of p-MWCNTs, a-MWCNTs, f-MWCNTs and g-MWCNTs is presented in Figure 3A–D, respectively. The AC conductivity of the nanocomposites provides information of the connectivity and electron transport mechanism of the MWCNTs network in the polymeric matrix (see Supplementary Materials, Text S2) [51–53].

The composite containing 0.5 wt% p-MWCNTs in PMMA matrix (Figure 3A) exhibits frequency-dependent conductance and thus remains insulated and lies below the percolation threshold. The behaviour of the 0.5 wt% nanocomposite is essentially similar to the PMMA matrix, with the exception that its conductance is an order of magnitude larger. At low filler loading, the filler content is not sufficient to form a conductive network, therefore, AC conduction occurred through the tunneling current. Figure 3A shows that in nanocomposite containing 1% p-MWCNTs, there is a significant increase in conductance from $1.733 \times 10^{-10}$ to $2.817 \times 10^{-2}$ S at a frequency of 25 Hz. The increase in the AC conductivity is about 8 order of magnitude which indicates that the percolation threshold is between p-MWCNTs weight fraction of 0.5 and 1 wt%. When the p-MWCNTs weight fraction is above the percolation threshold, the nanotubes interconnected and formed the conductive pathways, and the leakage current is responsible for the increase in the AC conductance [54]. Thus, the addition of 1% p-MWCNTs into the PMMA matrix is sufficient to obtain nanocomposites requiring electrical discharge. It can be observed that AC conductance becomes frequency independent after percolation has been attained. The high aspect ratio of MWCNTs allowed the achievement of the percolation threshold at a low weight fraction. When the percolation threshold is reached, the rise in conductance is relatively small, and an electrical conductivity plateau is obtained on further increasing the wt% of p-MWCNTs in subsequent nanocomposites. As the p-MWCNTs concentration in nanocomposites increases from 0 to 10 wt%, the conductance rises by nine orders of

magnitude. The increasing weight fraction of nanotubes reduced the intertube distance, thereby allowed effective charge transport [55]. However, in the high-frequency region, the conductance of the samples (i.e., 5 and 10 wt% p-MWCNTs/PMMA) was found to decrease with an increase in the frequency. In this high-frequency region, the electron hopping processmay be obstructed by the applied field [56,57], or the drop in the high-frequency region may also indicate that the measurements were outside the upper experimental range of the LCR meter used.
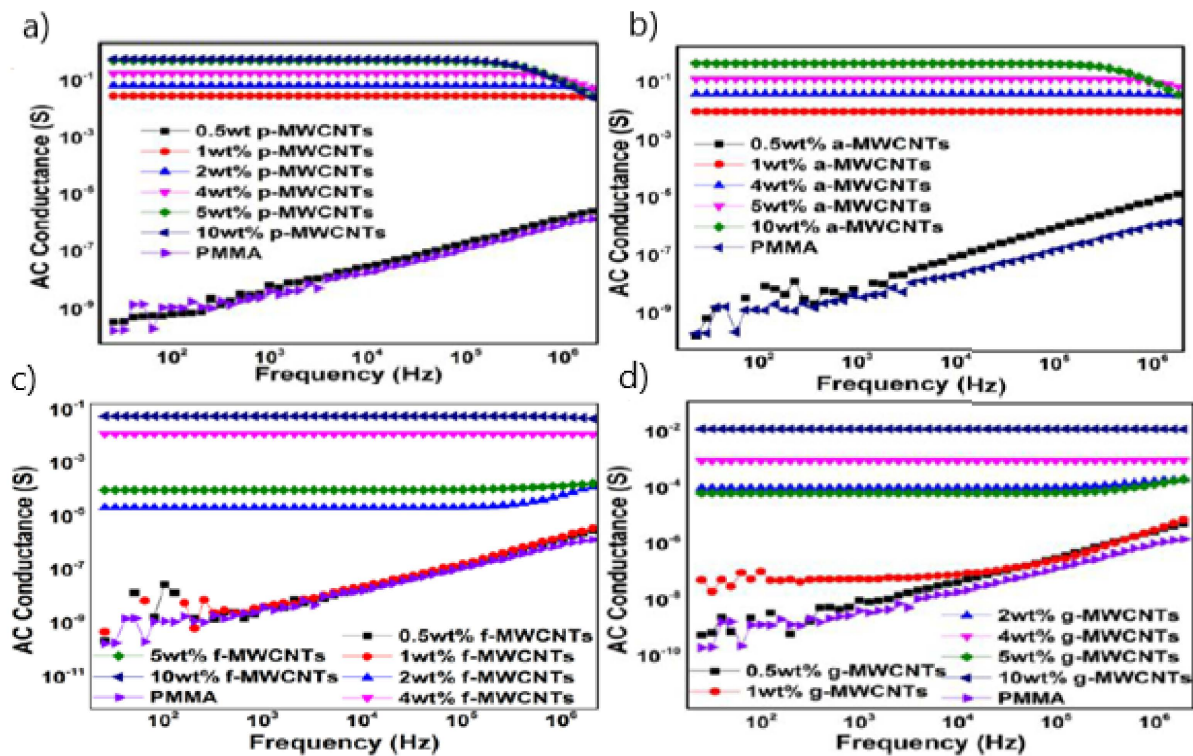


**Figure 3.** AC electrical conductance versus frequency for (**a**) p-MWCNTs/PMMA (**b**) a-MWCNTs/PMMA (**c**) f-MWCNTs/PMMA and (**d**) g-MWCNTs/PMMA nanocomposites as a function of different weight fractions of p-MWCNTs, a-MWCNTs, f-MWCNTs and g-MWCNTs, respectively.

The result for AC electrical conductance versus frequency for a-MWCNTs/PMMA nanocomposites of different weight percentages of a-MWCNTs is presented in Figure 3B. The same frequency dependence behavior is seen for a sample containing below 1 wt% a-MWCNTs. At 0.5 wt%, the nanocomposite remains an insulator. A significant increase in conductance was observed at 1 wt% p-MWCNTs/PMMA sample. The increase in the electrical conductance was 7 orders of magnitude, from $1.733 \times 10^{-10}$ to $8 \times 10^{-3}$ S for 1 wt% a-MWCNTs/PMMA sample relative to neat PMMA at 25 Hz frequency, which corresponds to DC electrical conductance. When the weight fraction increased from 1 to 5 wt%, an increase of 2 orders was found. As the concentration of a-MWCNTs increases from 0 to 10 wt% in the nanocomposite, the total increase in conductance was 9 orders of magnitude.

The AC electrical conductance vs. frequency of f-MWCNTs/PMMA nanocomposites for various weight fractions of f-MWCNTs is demonstrated in Figure 3C. The figure showed that nanocomposites with 0.5 and 1 wt% f-MWCNTs lie below the percolation threshold and remain nonconductive as they exhibit frequency-dependent behavior. The nanocomposite with 2 wt% f-MWCNTs exhibits a significant increase in electrical conductance from $1.733 \times 10^{-10}$ to $2.0 \times 10^{-5}$ S at a frequency of 25 Hz, which is about five orders of magnitude. The total increase in electrical conductance (as the weight fractions of f-MWCNTs increases from 0 to 10 wt%) was eight orders of magnitude. The conductance values of the nanocomposite containing 2 wt% f-MWCNTs do not vary (stay constant) with increas-

ing frequency up to a specified frequency in the high-frequency region beyond which an increase in electrical conductance was observed. Such behavior can be explained by modeling the complex admittance, Y, as a capacitor and resistor in parallel as defined by Equation (1).

$$Y(\omega) = Y' + Y'' = \frac{1}{R} + j\omega C \tag{1}$$

where $R$ is the resistance, $C$ is the capacitance, and $\omega$ is the angular frequency ($\omega = 2\pi f$), where $f$ is frequency. The AC electrical conductivity $\sigma_{AC}(\omega)$ is equal to Equation (2).

$$\sigma_{AC}(\omega) = |Y(\omega)| \frac{t}{A} \tag{2}$$

where $t$ is the thickness of the sample and $A$ is the area of the electrode. The DC electrical conductivity, $\sigma_{DC}$, is given by Equation (3).

$$\sigma_{DC} = Y' \frac{t}{A} \tag{3}$$

The result in Figure 3C can be explained by the resistor-capacitor model. The above equations show that the ohmic behavior, $1/R$, and the frequency induced dielectric behavior, $j\omega C$, contribute to the total AC electrical conductance. When the weight fraction of f-MWCNTs is below the percolation threshold, the impact of $Y'$ is very reduced due to a lack of conductivity networks, and hence $Y''$ controls the AC conductivity. The dielectric material acts as a capacitor due to this frequency dependency. After percolation, the charge carriers begin to flow across the conductive networks and ohmic behavior takes over [53,58]. As a result, the real component of admittance controls the conductivity, while the influence of frequency is only significant at higher frequency levels.

The variation in AC conductance of g-MWCNTs/PMMA nanocomposites with frequency for various weight fractions of g-MWCNTs is presented in Figure 3D. The nanocomposites containing 0.5 and 1 wt% g-MWCNTs remain nonconducting and exhibit frequency-dependent behavior. A significant increase of five orders of magnitude was found in electrical conductance for a sample containing 2 wt% g-MWCNTs as compared to neat PMMA, i.e., from $1.733 \times 10^{-10}$ to $8.8 \times 10^{-5}$ S at 25 Hz. This indicates that the percolation threshold is between 1 and 2 wt% samples. As the concentration increases from 0 to 10% g-MWCNTs, the total increase in conductance was about eight orders of magnitude. Figure 4A shows the comparative behavior of the variation of electrical conductance with frequency for p-MWCNTs (4 wt%)/PMMA, a-MWCNTs(4wt%)/PMMA, f-MWCNTs(4 wt%)/PMMA, and g-MWCNTs (4 wt%)/PMMA nanocomposites. The g-MWCNTs exhibited the lowest values of electrical conductivity, which may be attributed to the coating of the individual nanotubes by a grafted polymer. MWCNTs coated with the insulating surface not only contribute to dispersion but also result in poor electrical contact between nanotubes.

The comparative variation of AC conductance with frequency for PHB/p-MWCNTs (4 wt%)/PMMA, PHB/a-MWCNTs(4 wt%)/PMMA, PHB/f-MWCNTs(4wt%)/PMMA and PHB/g-MWCNTs(4 wt%)/PMMA nanocomposites are shown in Figure 4B. The addition of PHB to MWCNTs results in an insulating covering. As a result, the barrier gap for MWCNTs widens even more. Consequently, MWCNTs cannot connect directly to each other, which induces the lower AC conductance of PHB/MWCNTs(4 wt%)/PMMA than MWCNTs(4 wt%)/PMMA nanocomposites. The composites incorporating f-MWCNTs and g-MWCNTs had the lowest AC conductance values of all the nanocomposites examined (see Supplementary Materials, Table S1). This is likely due to their good interaction and dispersion in the polymeric blend. These findings are also supported by FTIR and SEM research.
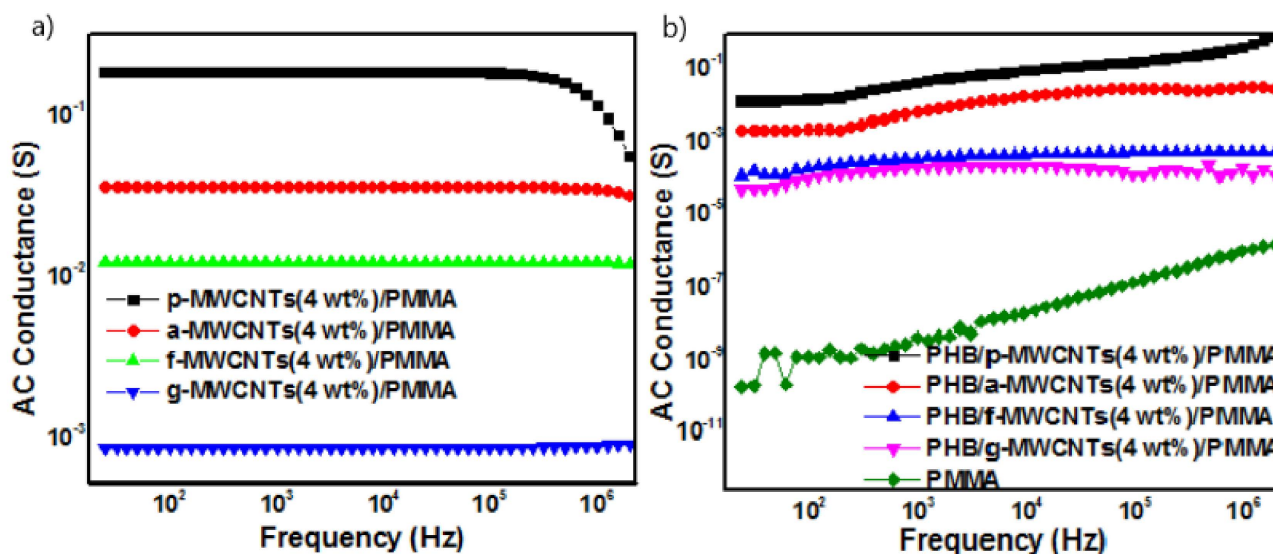
**Figure 4.** AC electrical conductance as a function of frequency for (**a**) MWCNTs(4 wt%)/PMMA nanocomposites. (**b**) variation of AC conductance with frequency for PHB/MWCNTs(4 wt%)/PMMA nanocomposites.

Energy Storage Properties

The ability of the synthesized nanocomposites to store energy in the form of electric charge can be measured with respect to their capacitance. All MWCNTs/PMMA containing p-MWCNTs and a-MWCNTs exhibit lower capacitance than the capacitance of neat PMMA [Figure 5a,b]. However, in f-MWCNTs/PMMA, the capacitance values of all composites containing f-MWCNTs are higher than neat PMMA except for 5 wt% and 10 wt% f-MWCNTs/PMMA nanocomposites (Figure 5c). In g-MWCNTs/PMMA nanocomposites the capacitance values of all studied compositions are higher than the neat PMMA except for the nanocomposite containing 10 wt% g-MWCNTs (Figure 5d). The variation of capacitance with frequency for p-MWCNTs(4 wt%)/PMMA, a-MWCNTs (4 wt%)/PMMA, f-MWCNTs(4 wt%)/PMMA and g-MWCNTs(4 wt%)/PMMA depicts that among all nanocomposites containing differently functionalized MWCNTs, f-MWCNTs (4 wt%)/PMMA exhibits higher capacitance values than that of PMMA (Figure 6a). The frequency capacitance of the PHB/p-MWCNTs(4 wt%)/PMMA, PHB/a-MWCNTs(4 wt%)/ PMMA, PHB/f-MWCNTs(4 wt%)/PMMA and PHB/g-MWCNTs(4 wt%)/PMMA are compared in Figure 6b. The capacitance values of PHB/MWCNTs/PMMA show that the composites containing f-MWCNTs and g-MWCNTs exhibit slightly higher capacitance values. The composites with capacitance values higher than neat PMMA are capable of storing electrical energy and can be used in electronic power devices [59]. The capacitance values of 2 wt% and 5 wt% g-MWCNTs/PMMA and 5 wt% f-MWCNTs/PMMA nanocomposites showed a decreasing trend with increasing frequency. The decrease in capacitance is because dipoles' relaxation is unable to reach equilibrium with electric field variation at different frequencies [60]. However, the increase in the capacitance with frequency may be due to the development of microcapacitors in the polymer matrix of dielectric materials when neighboring nanotubes are disconnected by a thin polymer [61]. Figure 5d depicted that increasing the wt% of g-MWCNTs in the PMMA matrix increases the microcapacitors formation with an increase in effective capacitance. This enhancement may be due to the polarization effects through the buildup of charges at the interfaces of the heterogeneous dielectric material according to Maxwell Wagner Sillar's theory. However, the lower capacitance value of g-MWCNTs(10 wt%)/PMMA than neat PMMA may be due to the agglomeration of MWCNTs in the polymeric matrix. The creation of the conductive network grows as the filler content increases, resulting in substantial current leakage. Nanocomposites including f-MWCNTs (Figure 5c) and g-MWCNTs (Figure 5d) have higher frequency capacitance than nanocomposites containing p-MWCNTs (Figure 5a) and a-MWCNTs

(Figure 5b). This emphasizes the importance of uniform dispersion and strong interfacial adhesion, which may be achieved by modifying MWCNTs, for nanocomposites to have significant energy storage capacity. However, the addition of PHB to MWCNTs/PMMA nanocomposites (Figure 6b) had no discernible influence on capacitance values.
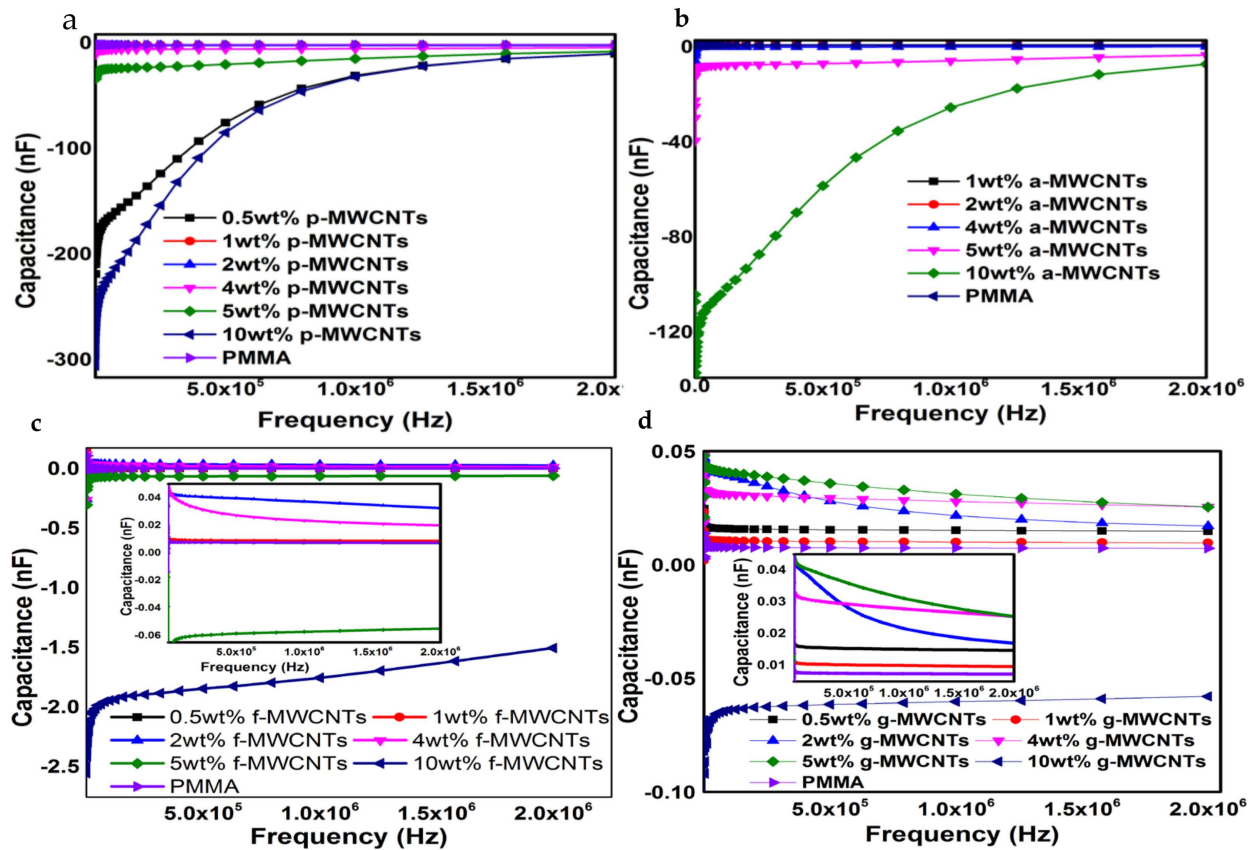


**Figure 5.** Capacitance versus frequency for (**a**) p-MWCNTs/PMMA (**b**) a-MWCNTs/PMMA (**c**) f-MWCNTs/PMMA and (**d**) g-MWCNTs/PMMA at different weight fractions of p-MWCNTs, a-MWCNTs, f-MWCNTs, and g-MWCNTs/PMMA.
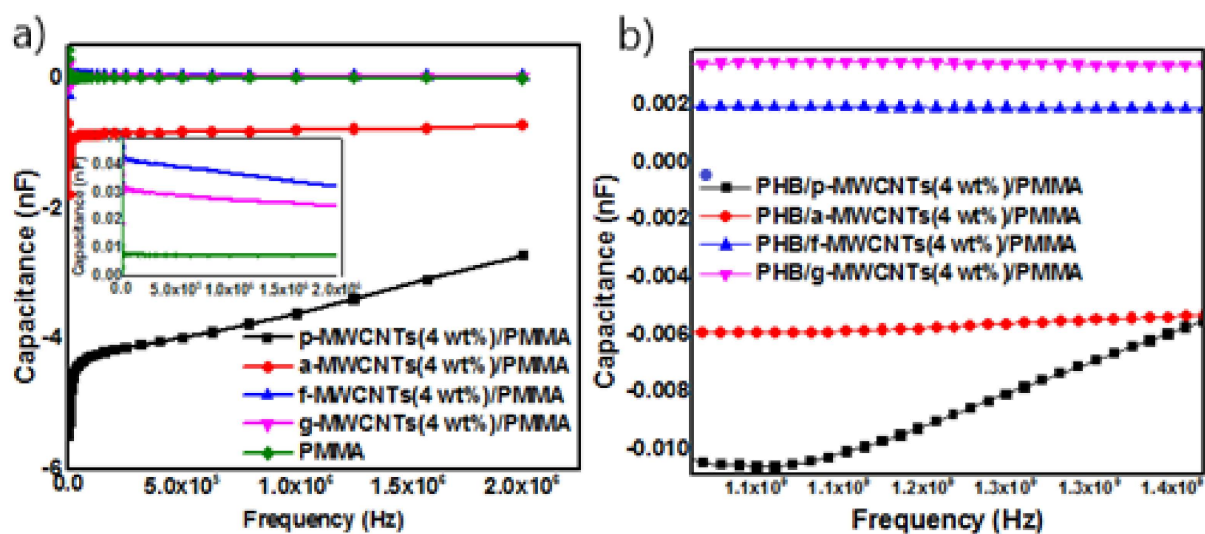


**Figure 6.** Capacitance as a function of frequency for (**a**) MWCNTs(4 wt%)/PMMA and (**b**) 411 PHB/MWCNTs (4 wt%)/PMMA.

### 3.4. Thermogravimetric Analysis (TGA)

The TGA and dTGA curves for PMMA and MWCNTs(4 wt%)/PMMA nanocomposites are presented in Figure 7A,B. The derivative thermogravimetric (dTGA) results were acquired by taking the time derivative of the ratio of the sample weight (W) to the initial sample weight ($W_o$), $d(W/W_o)/dt$ [62]. Figure 7B shows that the complete degradation of PMMA occurs at ≈ 396 °C. In dTGA of PMMA two minor degradation steps appeared at 157 and 287 °C. A major degradation step also appeared at 368 °C. This result is consistent with earlier published data [63–65]. The first peak corresponds to the decomposition of the weak head to head bonds arising from chain termination by the combination [66]. It may also predict the presence of solvent in polymer film [67]. The second one may correspond to the transfer of radicals tomonomers [68]. The third peak of thermal decomposition is due to the random scission of the PMMA backbone [62,69]. The peak height increases with an increase in temperature [65].
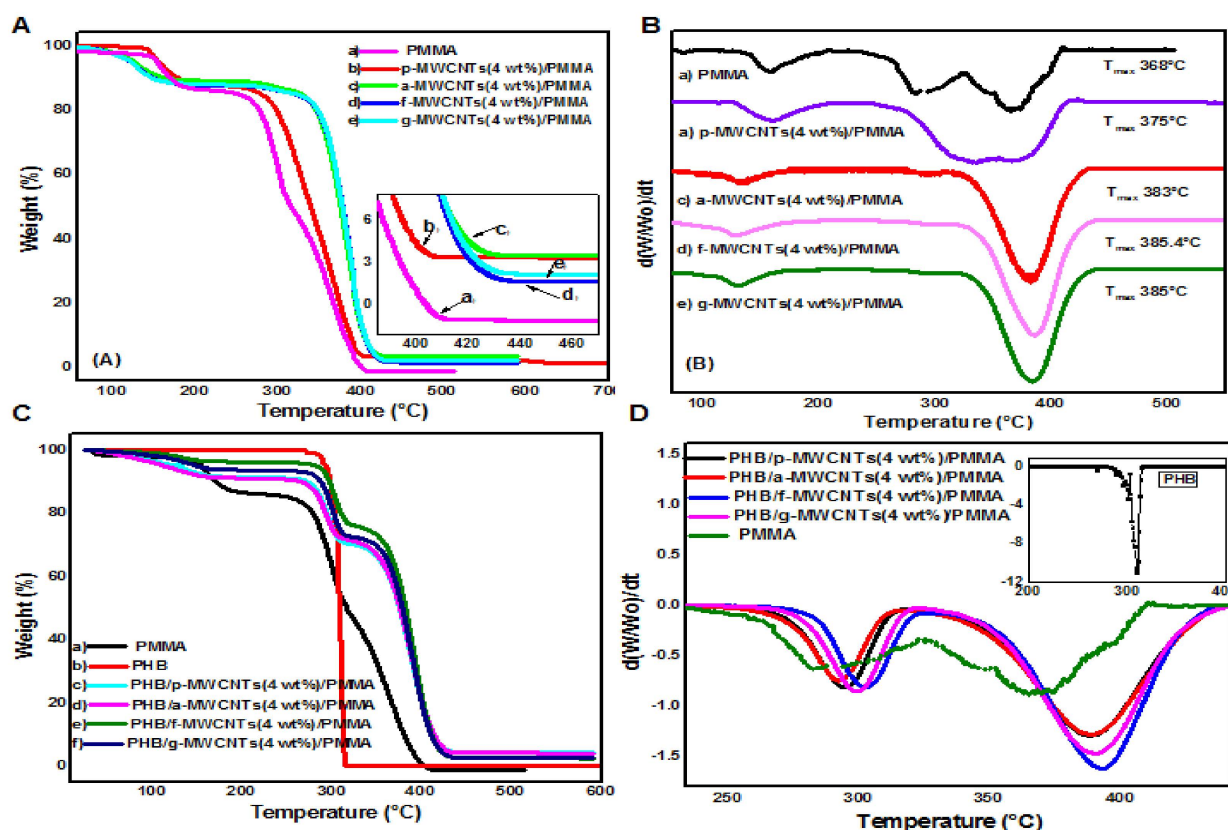


**Figure 7.** Comparison of (**A**) TGA and (**B**) dTGA curves for PMMA and PMMA(4 wt%)/MWCNTs nanocomposites. (**C**) TGA and (**D**) dTGA profiles of PMMA and PHB/MWCNTs(4 wt%)/PMMA nanocomposites. The inset graph shows the dTGA curve of PHB.

Different parameters regarding thermal stability were calculated such as temperature at 5% weight loss (T5), temperature at 10% weight loss (T10), temperature at 50% weight loss (T50), maximum degradation temperature (Tmax), complete degradation temperature (Tend) and residual material at 400 °C. The relative thermal stability of all synthesized nanocomposites was assessed by comparing T5, T10, T50, Tmax, Tend and the amount of residual material remaining at 400 °C. Thermogravimetric data analyses of all the synthesized nanocomposites along with neat PMMA and PHB are reported in Table 1. Data analysis showed that the addition of pristine MWCNTs, as well as differently functionalized MWCNTs in PMMA alone and in the PHB/PMMA blend system, increases its thermal stability. T50, Tmax and Tend for nearly all the composites is shifted towards high temperature as compared to neat PMMA and PHB. Polymer chains may degrade more slowly near MWCNTs, which may delay the

degradation temperature to high values. The thermal stability of nanocomposites is enhanced due to the greater thermal conductivity of MWCNTs, which promotes heat dissipation in the nanocomposites [70].

**Table 1.** TGA and dTGA data of MWCNTs(4 wt%)/PMMA and PHB/MWCNTs/PMMA nanocomposites.

| Samples | T5/°C | T10/°C | T50/°C | Tmax/°C | Tend/°C | Residual Material at 400 °C |
|---|---|---|---|---|---|---|
| PMMA | 154 | 170 | 317 | 368 | 396 | 1.07% |
| PHB | - | - | - | - | 314 | 0% |
| p-MWCNTs(4 wt%)/PMMA | 156.8 | 180.4 | 339.4 | 375 | 395 | 4.4% |
| a-MWCNTs(4 wt%)/PMMA | 128 | 163.5 | 375.7 | 383 | 411 | 15% |
| f-MWCNTs(4 wt%)/PMMA | 123 | 150.31 | 378.2 | 385.4 | 414 | 16% |
| g-MWCNs(4 wt%)/PMMA | 123 | 148.4 | 378 | 385 | 414 | 17% |
| PHB/p-MWCNTs(4 wt%)/PMMA | 123.5 | 271.3 | 376 | 388.6 | 425 | 21% |
| PHB/a-MWCNTs(4 wt%)/PMMA | 113 | 264 | 339.4 | 389 | 425 | 22% |
| PHB/f-MWCNTs(4 wt%)/PMMA | 281 | 296 | 382.5 | 393 | 424 | 23% |
| PHB/g-MWCNs(4 wt%)/PMMA | 149 | 287 | 379 | 390 | 424 | 21% |

The dTGA curves (Figure 7B(b–e)) of MWCNTs(4 wt%)/PMMA nanocomposites show strong suppression of the peak at 287 °C. This indicates that in the presence of MWCNTs, the transfer of PMMA radicals to monomers is significantly suppressed. The data in Table 1 shows that the addition of f-MWCNTs and g-MWCNTs to the PMMA matrix has a substantial effect on the improvement of thermal stability at T50 (up to 61 degrees). An increase in the temperature at complete degradation (about 18 degrees) is shown in an expanded view of the TGA curves (380–460 °C) in Figure 7A(f,g). The good thermal stability of modified MWCNTs based nanocomposites is associated with their better dispersion in the matrix PMMA since it hinders the flux of degradation product and hence delays the decomposition process. It may be concluded that the thermal stability depends upon the difference in the extent of interaction between PMMA and modified MWCNTs, consequently. After complete decomposition, all the organiccontent removes from the sample and only carbon nanotube with a small amount of residue is left. The data given in Table 1 shows that the degradation temperature of f-MWCNTs(4 wt%)/PMMA and g-MWCNTs(4 wt%)/PMMA based nanocomposite at 5% weight loss (T5) and 10% weight loss (T10) shifted towards lower temperature values (up to 31 degrees). This reduction in T5 and T10 values are supported by the structural defects on the surface of MWCNTs upon functionalization as well as thermal degradation of carboxylic acid groups and 4,4-diaminodiphenyl sulphone moieties besides the decomposition of weak linkages in PMMA.

Figure 7C,D show TGA and dTGA curves for PMMA, PHB and PHB/MWCNTs (4 wt%)/PMMA nanocomposites. Figure 7C(b) shows that PHB decomposes in a single stage between 274 and 315 °C, with strong molecular structural stability up to 260 °C. The second step in TGA curves (Figure 7C(c–f)) for all PHB/MWCNTs(4 wt%)/PMMA nanocomposites indicates the thermal degradation of PHB. Figure 7D(a–d) shows the evident shift in dTGA curves of PHB/MWCNTs(4 wt%)/PMMA composites towards high temperature as compared to neat PMMA (Figure 7D(e)). Data in Table 1 depict that incorporation of PHB further improves the thermal stability of nanocomposites. However, PHB/f-MWCNTs(4 wt%)/PMMA blend system shows good thermal properties among all the synthesized nanocomposites. In comparison to neat PMMA, results from TGA and dTGA analyses of PHB/f-MWCNTs(4 wt%)/PMMA reveal a delay in T5 (about 127 °C), T50 (up to 126 °C) and Tmax(up to 65 °C) in contrast to. The improved thermal properties

may correspond to good miscibility and compatibility of f-MWCNTs in both polymers (i.e. PMMA and PHB). The compatibilization occurred by forming covalent bonds. Secondary interactions such as hydrogen bonding between the components of blend also played their role in imparting compatibilization. Secondary interaction may occur because of interactive functional groups introduced on the sidewalls of MWCNTs [71]. The hydrophobic nature of PHB could explain the highest delay in T5 and T10. In its molecular structure, PHB absorbs the least quantity of moisture [72]. This hydrophobic property is especially noticeable in composites with high MWCNTs dispersion. As a result, MWCNTs are surrounded by polymer chains, reducing the weight loss caused by moisture. However, the little proportion of weight may be related to the deterioration of PMMA's poor head-to-head connections.

### 3.5. Analysis of Ammonia Gas Sensing Properties

The sensitivity (S) can be determined by following Equation (4).

$$S = \frac{Ri - R^\circ}{R^\circ} \times 100 \tag{4}$$

where $Ri$ is the resistance of the sensor in ammonia and $R^\circ$ is the resistance of the sensor in the air. The response and recovery time is defined as the time of 90% total sensor's resistance change.

LOD is calculated by using Equation (5).

$$LOD = 3S_D/m \tag{5}$$

where m is the slope of calibration curve. $S_D$ corresponds to the standard deviation of noise in the response curve in dry air.

### 3.5.1. PMMA/MWCNTs Nanocomposites based Ammonia Gas Sensors

The p-MWCNTs(4 wt%)/PMMA, a-MWCNTs(4 wt%)/PMMA, f-MWCNTs(4 wt%)/ PMMA and g-MWCNTs(4 wt%)/PMMA sensors were exposed to increasing concentrations of ammonia vapors. An increase in the electrical resistance was observed as shown in Figure 8a–d. This increase in the electrical resistance is attributed to the fact that polar $NH_3$ molecules interact through hydrogen bonding with oxygen functionalities present on the sidewall MWCNTs. Ammonia is a reducing gas and transfers electron(s) to the p-type MWCNTs. The transferred electron(s) recombines with 'hole' carriers in p-type MWCNTs, depleting charge carrier holes and raising the electrical resistance [73]. Due to the adsorption of gas molecules, the volume of the PMMA matrix changes which inturn increases the intertube distance. As a result, the resistance increases [74]. The higher sensitivity of the g-MWCNTs(4 wt%)/PMMA sensor can be attributed to the greater interaction of ammonia with g-MWCNTs, as shown in Figure 9. Figure 10a–d show the response of the gas sensors after being exposed to ammonia gas periodically. The g-MWCNTs(4 wt%)/PMMA nanocomposites [Figure 10d] had a good reversible reaction to ammonia vapors.
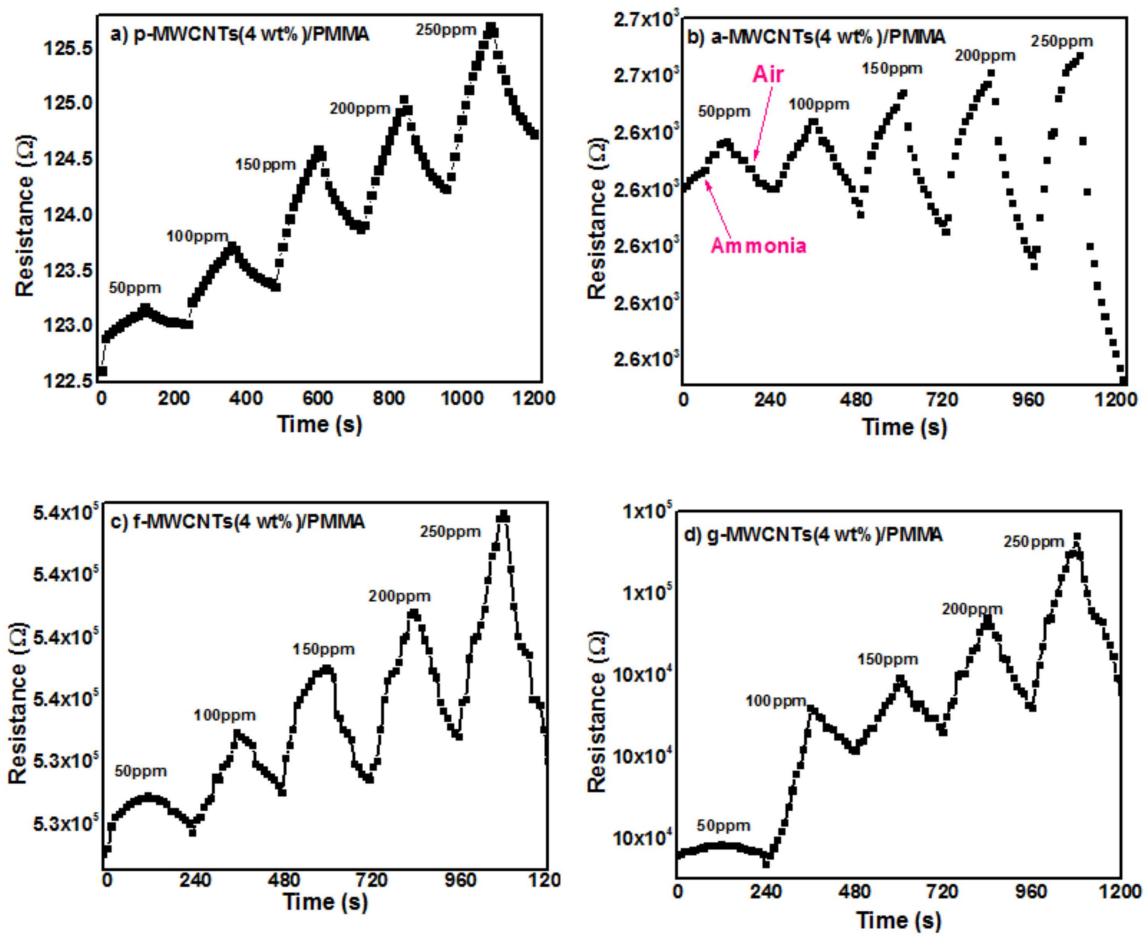
**Figure 8.** Response of (**a**) p-MWCNTs(4 wt%)/PMMA, (**b**) a-MWCNTs(4 wt%)/PMMA, (**c**) f-MWCNTs(4 wt%)/PMMA and (**d**) g-MWCNTs(4 wt%)/PMMA nanocomposites to ammonia va-pors.
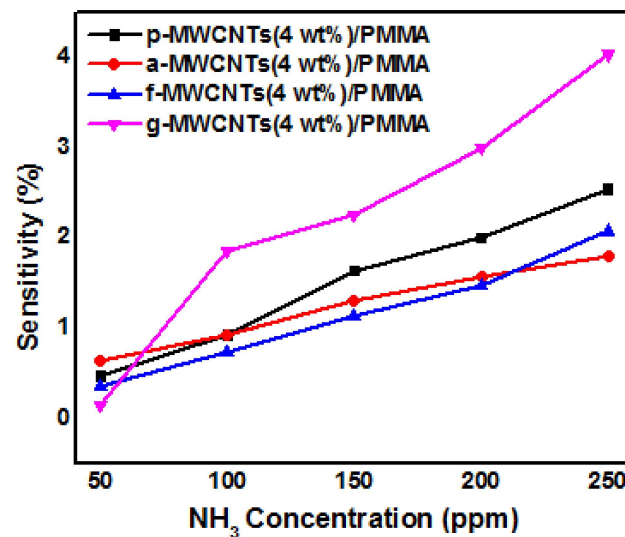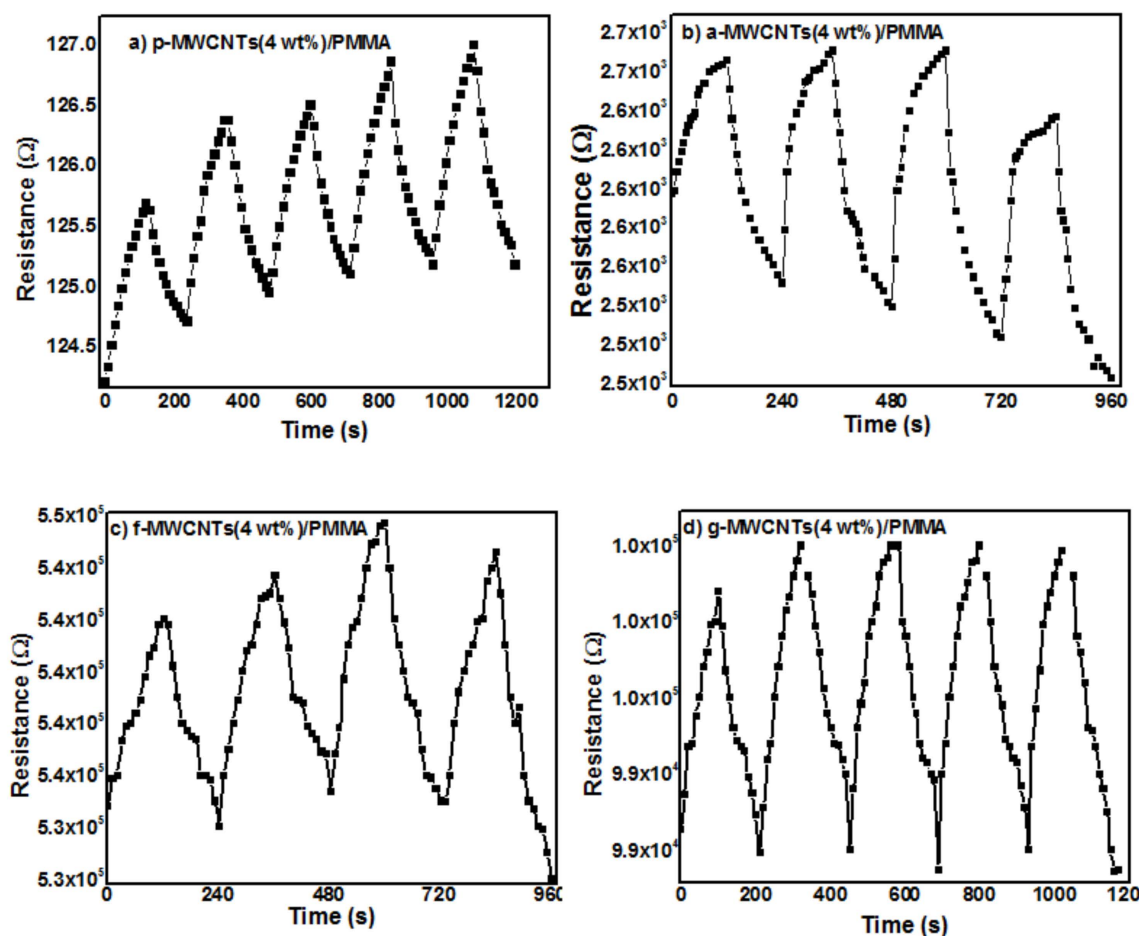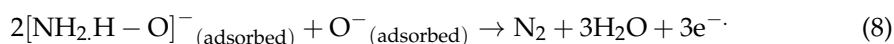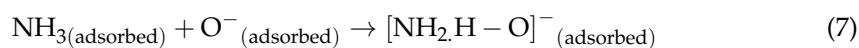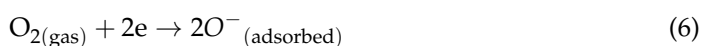


**Figure 9.** Sensitivity of p-MWCNTs(4 wt%)/PMMA (black line), a-MWCNTs(4 wt%)/PMMA (red line), f-MWCNTs(4 wt%)/PMMA (blue line) and g-MWCNTs(4 wt%)/PMMA (pink line) as a function of $NH_3$ concentration.
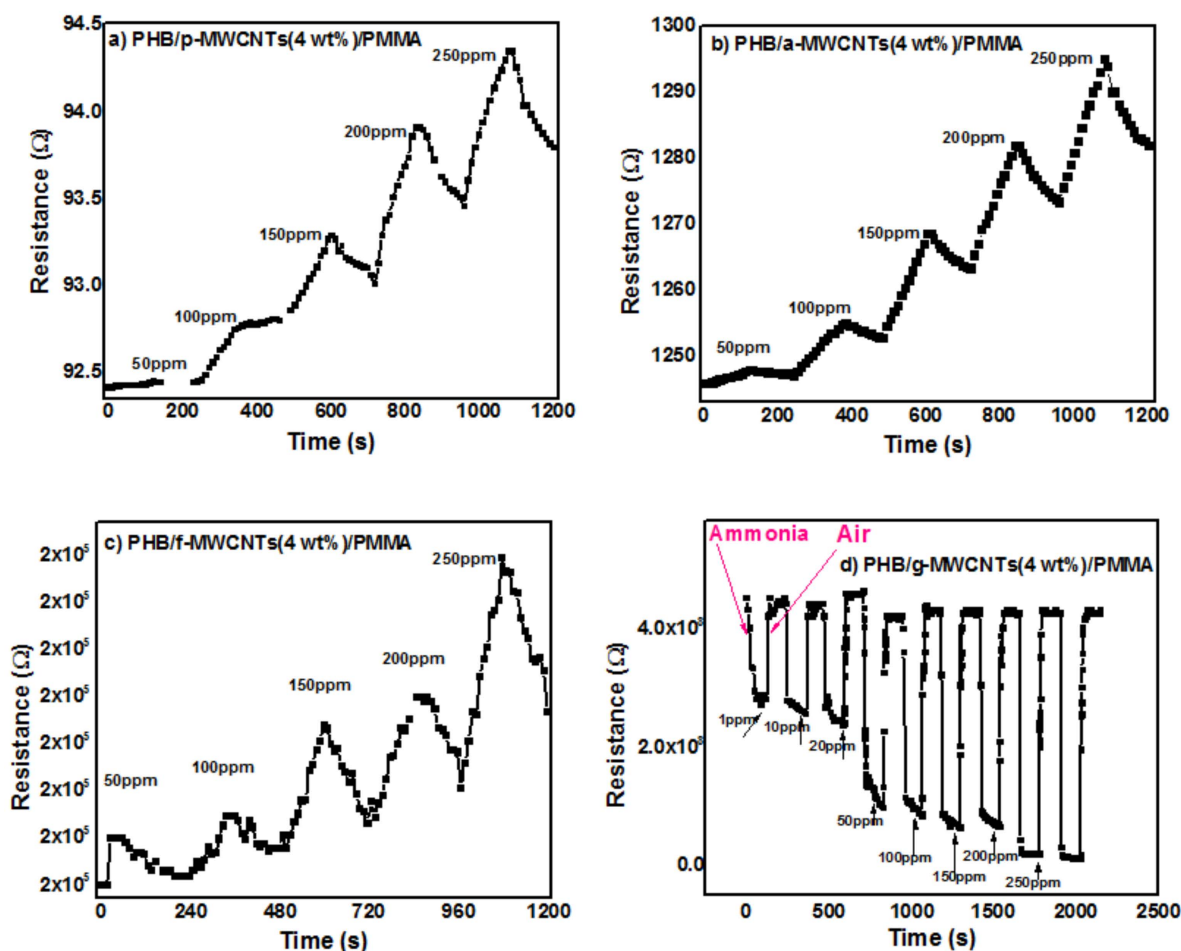
**Figure 10.** Cyclability of (**a**) p-MWCNTs(4 wt%)/PMMA, (**b**) a-MWCNTs(4 wt%)/PMMA, (**c**) f-MWCNTs(4 wt%)/PMMA and (**d**) g-MWCNTs(4 wt%)/PMMA nanocomposites to ammonia vapors at 250 ppm.

### 3.5.2. PMMA/MWCNTs(4 wt%)/PHB Nanocomposites based Ammonia Gas Sensors

The response of PHB/p-MWCNTs(4 wt%)/PMMA, PHB/a-MWCNTs(4 wt%)/PMMA, PHB/f-MWCNTs(4 wt%)/PMMA and PHB/g-MWCNTs(4 wt%)/PMMA sensors to various concentrations of ammonia are shown in Figure 11a–d. Except for PHB/g-MWCNTs (4 wt%)/PMMA sensor, all the synthesized nanocomposites showed an increase in resistance following exposure to ammonia (Figure 11a–c). When exposed to ammonia, the PHB/g-MWCNTs(4 wt%)/PMMA (Figure 11d) sensor displayed a decreasing trend in resistance, which is trivial for an n-type semiconductor. Both the amine groups [75] and PHB [76] act as electron donors, effectively converting MWCNTs to n-type semiconductors. Since g-MWCNTs are uniformly dispersed in the polymeric matrix, they interact well with PHB, resulting in a greater number of g-MWCNTs coming into physical contact with the electron-donating PHB molecules, allowing for more effective doping. In n-type semiconductors, electrons are the primary charge carriers [77]. The sensor material adsorbed oxygen molecules from the air (Equation (6)). The charge carriers (i.e., electrons) in n-type semiconductors supports the formation of charged oxygen species.

$$O_{2(gas)} + 2e \rightarrow 2O^-_{(adsorbed)} \tag{6}$$

$$NH_{3(adsorbed)} + O^-_{(adsorbed)} \rightarrow [NH_2.H - O]^-_{(adsorbed)} \tag{7}$$

$$2[NH_2.H - O]^-_{(adsorbed)} + O^-_{(adsorbed)} \rightarrow N_2 + 3H_2O + 3e^-. \tag{8}$$

**Figure 11.** Response of (**a**) PHB/p-MWCNTs(4 wt%)/PMMA, (**b**) PHB/a-MWCNTs(4 wt%)/PMMA, (**c**) PHB/f-MWCNTs (4 wt%)/PMMA and (**d**) PHB/g-MWCNTs(4 wt%)/PMMA nanocomposites to ammonia vapors.

However, depletion of electron concentration increases resistance. Ammonia onexposure to PHB/g-MWCNTs(4 wt%)/PMMA, interacts with its lone pair of electrons to the interacting sites present in the porous surface [78]. Then, the absorbed ammonia molecules interact with charged oxygen species subsequently, releasing N2 and water (Equations (7,8)). The captured electrons are released into the conduction band, resulting in an increase in the concentration of charge carriers in the sample. The increase in charge carrier concentration is proportional to the decrease in the resistance [79].

SEM studies revealed the highly porous morphology of PHB/g-MWCNTs(4 wt%)/ PMMA nanocomposites. Due to the porous nature of the sample, gas can diffuse into and out of the nanocomposites quickly and shortens the response and recovery time consequently. The enhanced performance of PHB/g-MWCNTs(4 wt%)/PMMA in the response time and sensitivity was due to its higher effective surface area. The gas carriers also desorbed the analyte from the porous structure more quickly, as shown in Figure 11d. LOD calculated for PHB/g-MWCNTs(4 wt%)/PMMA is 0.129 ppm while the detection limit of all other nanocomposites is above 40 ppm. PHB/g-MWCNTs (4 wt%)/PMMA showed linear sinsitivity in 1–50 ppm range. The performance of the PHB/g-MWCNTs(4 wt%)/PMMA sensor outperforms that of earlier MWCNTs-based composites. Sahal et al. [80] reported a linear sensitivity of 5–20 ppm for a PANI/PMMA/PS/ MWCNTs ammonia sensor with 0.830 ppm LOD. Marity and Ramasamy et al. [81] synthesized MWCNTs/PANI fabric sensor and reported 0.200 ppm LOD. For HCSA-doped PANI:CNTs, Marcelo and Carlos et al. [82] reported 4 ppm LOD. The sensitivity comparison of the PHB/p-MWCNTs(4 wt%)/PMMA, PHB/a-MWCNTs(4 wt%)/PMMA, PHB/f-MWCNTs(4 wt%)/PMMA and PHB/g-MWCNTs(4 wt%)/PMMA (inset) is shown

in Figure 12. Figure 12 demonstrates that when compared to all other synthesized nanocomposite sensors, PHB/g-MWCNTs(4 wt%)/PMMA sensors have a 20-fold increase in sensitivity ($\approx$100%). The PHB/g-MWCNTs(4 wt%)/PMMA sensor in the inset of Figure 12 also depicts excellent sensitivity when exposed to low concentrations of $NH_3$ as compared to other nanocomposites. All the fivesets of the gas sensors were also examined under continuous exposure of ammonia gas (250 ppm) at room temperature (Figure 13a–d). Only PHB/g-MWCNTs(4 wt%)/PMMA (Figure 13d) displays outstanding repeatability with a steady response up to five cycles. The explanation for this could be related to the porous structure created by wrapping g-MWCNTs in a PMMA/PHB blend. The porous construction allows for easy ammonia gas diffusion, resulting in rapid reaction and good reversibility.
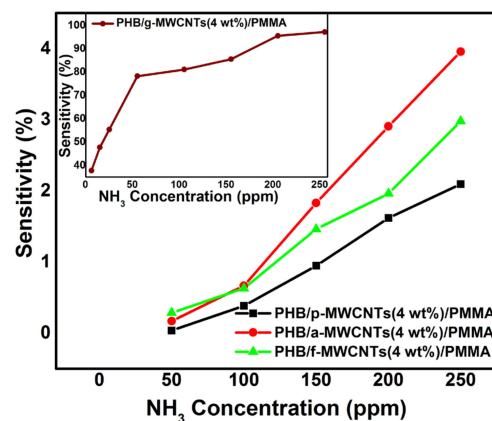


**Figure 12.** Sensitivity of PHB/p-MWCNTs(4 wt%)/PMMA (black line), PHB/a-MWCNTs (4 wt%)/PMMA (red line) and PHB/f-MWCNTs(4 wt%)/ PMMA (green line). Inset shows the sensitivity of PHB/g-MWCNTs(4 wt%)/ PMMA (brown line) as a function of $NH_3$ concentration.
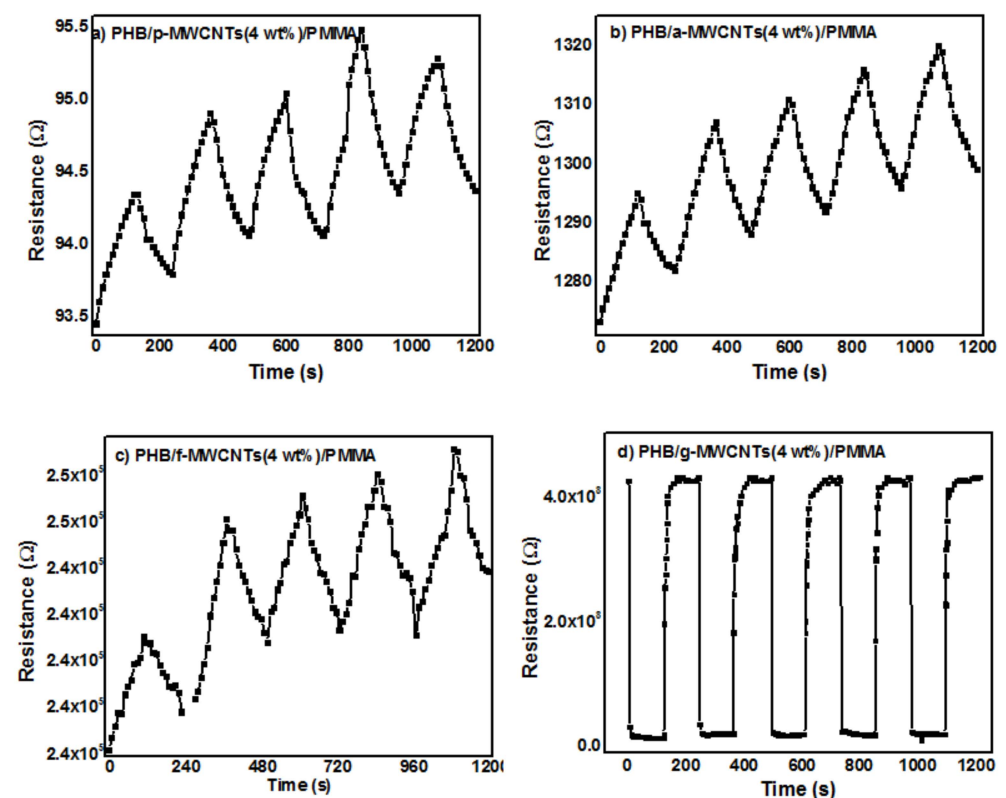


**Figure 13.** Cyclability of (**a**) PHB/p-MWCNTs(4 wt%)/PMMA, (**b**) PHB/a-MWCNTs(4 wt%)/PMMA, (**c**) PHB/f-MWCNTs(4 wt%)/PMMA and (**d**) PHB/g-MWCNTs(4 wt%)/PMMA nanocomposites to ammonia vapors at 250 ppm.

## 4. Conclusions

The surface functionalization of MWCNTs resulted in uniform distribution and robust interfacial interactions with PMMA alone and a PHB/PMMA blend, according to FTIR and SEM studies. The integration of f-MWCNTs and g-MWCNTs in PMMA and PHB/PMMA could significantly improve the energy storage capability, according to a capacitance test conducted on nanocomposites. As a result, the fabricated nanocomposites i.e., f-MWCNTs(4wt%)/PMMA, g-MWCNTs(4 wt%)/PMMA, PHB/f-MWCNTs (4 wt%)/PMMA, PHB/g-MWCNTs(4 wt%)/PMMA are expected to find application as the capacitor materials. In comparison to the neat PMMA dielectric capacitor, the dielectric nanocomposites' increased capacitance will boost the energy storage capacity. Nanocomposites including functionalized MWCNTs (f-MWCNTs and g-MWCNTs) have better thermal properties than those containing p-MWCNTs, according to the thermogravimetric study. The greater dispersion of MWCNTs is responsible for the increase in the thermal degradation temperature of nanocomposites as compared to neat PMMA and PHB. As a result, functionalization is a necessary step in the reinforcement effectiveness. MWCNTs in nanocomposites act as restriction sites, reducing the segmental mobility of polymeric chains. The lower mobility helps to improve the thermal stability of nanocomposites by delaying chain scission [83]. PHB/f-MWCNTs(4 wt%)/PMMA and PHB/g-MWCNTs (4 wt%)/PMMA nanocomposites have improved thermal stability, making them ideal materials for synthesizing high-performance nanocomposites. Among the nanocomposites PHB/g-MWCNTs(4 wt%)/PMMA showed better ammonia sensing response. The sensor has a high sensitivity for detecting ammonia (97% for 250 ppm).

## References

1. Choudhary, V.; Gupta, A. Polymer/carbon nanotube nanocomposites. *Carbon Nanotub.-Polym. Nanocomposites* **2011**, *2011*, 65–90.
2. Bezzon, V.D.; Montanheiro, T.L.; de Menezes, B.R.; Ribas, R.G.; Righetti, V.A.; Rodrigues, K.F.; Thim, G.P. Carbon nanostructure-based sensors: A brief review on recent advances. *Adv. Mater. Sci. Eng.* **2019**, *2019*, 1–21. [CrossRef]

3. Bajpai, A.; Carlotti, S. The effect of hybridized carbon nanotubes, silica nanoparticles, and core-shell rubber on tensile, fracture mechanics and electrical properties of epoxy nanocomposites. *Nanomaterials* **2019**, *9*, 1057. [CrossRef] [PubMed]

4. Kidd, J.; Bi, Y.; Hanigan, D.; Herckes, P.; Westerhoff, P. Yttrium residues in MWCNT enable assessment of MWCNT removal during wastewater treatment. *Nanomaterials* **2019**, *9*, 670. [CrossRef]

5. Tamburri, E.; Orlanducci, S.; Terranova, M.; Valentini, F.; Palleschi, G.; Curulli, A.; Brunetti, F.; Passeri, D.; Alippi, A.; Rossi, M. Modulation of electrical properties in single-walled carbon nanotube/conducting polymer composites. *Carbon* **2005**, *43*, 1213–1221. [CrossRef]

6. Gong, S.; Zhu, Z.; Meguid, S. Anisotropic electrical conductivity of polymer composites with aligned carbon nanotubes. *Polymer* **2015**, *56*, 498–506. [CrossRef]

7. Sun, W.; Tomita, H.; Hasegawa, S.; Kitamura, Y.; Nakano, M.; Suehiro, J. An array of interdigitated parallel wire electrodes for preparing a large-scale nanocomposite film with aligned carbon nanotubes. *J. Phys. D Appl. Phys.* **2011**, *44*, 445303. [CrossRef]

8. Xie, X.-L.; Mai, Y.-W.; Zhou, X.-P. Dispersion and alignment of carbon nanotubes in polymer matrix: A review. *Mater. Sci. Eng. R Rep.* **2005**, *49*, 89–112. [CrossRef]

9. Tang, R.; Shi, Y.; Hou, Z.; Wei, L. Carbon nanotube-based chemiresistive sensors. *Sensors* **2017**, *17*, 882. [CrossRef]

10. Akyildiz, I.F.; Jornet, J.M. Electromagnetic wireless nanosensor networks. *Nano Commun. Netw.* **2010**, *1*, 3–19. [CrossRef]

11. Zaporotskova, I.V.; Boroznina, N.P.; Parkhomenko, Y.N.; Kozhitov, L.V. Carbon nanotubes: Sensor properties. A review. *Mod. Electron. Mater.* **2016**, *2*, 95–105. [CrossRef]

12. Klein, H.; Mani, K.A.; Chauhan, V.; Yaakov, N.; Grzegorzewski, F.; Domb, A.J.; Mechrez, G. Covalent Immobilization of Polyaniline Doped with $Ag^+$ or $Cu^{2+}$ on Carbon Nanotubes for Ethylene Chemical Sensing. *Nanomaterials* **2021**, *11*, 1993. [CrossRef]

13. Schroeder, V.; Savagatrup, S.; He, M.; Lin, S.; Swager, T.M. Carbon nanotube chemical sensors. *Chem. Rev.* **2018**, *119*, 599–663. [CrossRef] [PubMed]

14. Özütok, F.; Er, I.K.; Acar, S.; Demiri, S. Enhancing the Co gas sensing properties of ZnO thin films with the decoration of MWCNTs. *J. Mater. Sci. Mater. Electron.* **2019**, *30*, 259–265. [CrossRef]

15. Tserengombo, B.; Jeong, H.; Dolgor, E.; Delgado, A.; Kim, S. Effects of Functionalization in Different Conditions and Ball Milling on the Dispersion and Thermal and Electrical Conductivity of MWCNTs in Aqueous Solution. *Nanomaterials* **2021**, *11*, 1323. [CrossRef]

16. Den Hoed, F.; Pucci, A.; Picchioni, F.; Raffa, P. Design of a pH-responsive conductive nanocomposite based on MWCNTs stabilized in water by amphiphilic block copolymers. *Nanomaterials* **2019**, *9*, 1410. [CrossRef]

17. Lourie, O.; Wagner, H. Transmission electron microscopy observations of fracture of single-wall carbon nanotubes under axial tension. *Appl. Phys. Lett.* **1998**, *73*, 3527–3529. [CrossRef]

18. Moniruzzaman, M.; Winey, K.I. Polymer nanocomposites containing carbon nanotubes. *Macromolecules* **2006**, *39*, 5194–5205. [CrossRef]

19. Spitalsky, Z.; Tasis, D.; Papagelis, K.; Galiotis, C. Carbon nanotube–polymer composites: Chemistry, processing, mechanical and electrical properties. *Prog. Polym. Sci.* **2010**, *35*, 357–401. [CrossRef]

20. Bhattacharya, M. Polymer nanocomposites—A comparison between carbon nanotubes, graphene, and clay as nanofillers. *Materials* **2016**, *9*, 262. [CrossRef]

21. Kumar, A.; Sharma, K.; Dixit, A.R. Carbon nanotube-and graphene-reinforced multiphase polymeric composites: Review on their properties and applications. *J. Mater. Sci.* **2020**, *55*, 2682–2724. [CrossRef]

22. Vicentini, N.; Gatti, T.; Salerno, M.; Gomez, Y.S.H.; Bellon, M.; Gallio, S.; Marega, C.; Filippini, F.; Menna, E. Effect of different functionalized carbon nanostructures as fillers on the physical properties of biocompatible poly(l-lactic acid) composites. *Mater. Chem. Phys.* **2018**, *214*, 265–276. [CrossRef]

23. Haider, T.P.; Völker, C.; Kramm, J.; Landfester, K.; Wurm, F.R. Plastics of the future? The impact of biodegradable polymers on the environment and on society. *Angew. Chem. Int. Ed.* **2019**, *58*, 50–62. [CrossRef] [PubMed]

24. Avella, M.; Martuscelli, E.; Pascucci, B.; Raimo, M.; Focher, B.; Marzetti, A. A new class of biodegradable materials: Poly-3-hydroxy-butyrate/steam exploded straw fiber composites. I. Thermal and impact behavior. *J. Appl. Polym. Sci.* **1993**, *49*, 2091–2103. [CrossRef]

25. Macagnano, A.; Perri, V.; Zampetti, E.; Bearzotti, A.; De Cesare, F. Humidity effects on a novel eco-friendly chemosensor based on electrospun PANi/PHB nanofibres. *Sens. Actuators B Chem.* **2016**, *232*, 16–27. [CrossRef]

26. Kim, K.J.; Doi, Y.; Abe, H. Effects of residual metal compounds and chain-end structure on thermal degradation of poly(3-hydroxybutyric acid). *Polym. Degrad. Stab.* **2006**, *91*, 769–777. [CrossRef]

27. Pizzoli, M.; Scandola, M.; Ceccorulli, G. Crystallization and melting of isotactic poly(3-hydroxy butyrate) in the presence of a low molecular weight diluent. *Macromolecules* **2002**, *35*, 3937–3941. [CrossRef]

28. Pachekoski, W.M.; Agnelli, J.A.M.; Belem, L.P. Thermal, mechanical and morphological properties of poly(hydroxybutyrate) and polypropylene blends after processing. *Mater. Res.* **2009**, *12*, 159–164. [CrossRef]

29. Lai, S.M.; Sun, W.W.; Don, T.M. Preparation and characterization of biodegradable polymer blends from poly(3-hydroxybutyrate)/poly(vinyl acetate)-modified corn starch. *Polym. Eng. Sci.* **2015**, *55*, 1321–1329. [CrossRef]

30. Mousavioun, P.; Doherty, W.O.; George, G. Thermal stability and miscibility of poly(hydroxybutyrate) and soda lignin blends. *Ind. Crops Prod.* **2010**, *32*, 656–661. [CrossRef]

31. Soleymani Eil Bakhtiari, S.; Bakhsheshi-Rad, H.R.; Karbasi, S.; Tavakoli, M.; Razzaghi, M.; Ismail, A.F.; RamaKrishna, S.; Berto, F. Polymethyl methacrylate-based bone cements containing carbon nanotubes and graphene oxide: An overview of physical, mechanical, and biological properties. *Polymers* **2020**, *12*, 1469. [CrossRef]

32. Mishra, S.K.; Tripathi, S.N.; Choudhary, V.; Gupta, B.D. SPR based fibre optic ammonia gas sensor utilizing nanocomposite film of PMMA/reduced graphene oxide prepared by in situ polymerization. *Sens. Actuators B Chem.* **2014**, *199*, 190–200. [CrossRef]

33. Abou-Aiad, T. Morphology and dielectric properties of polyhydroxybutyrate (PHB)/poly(methylmethacrylate)(PMMA) blends with some antimicrobial applications. *Polym.-Plast. Technol. Eng.* **2007**, *46*, 435–439. [CrossRef]

34. He, Y.; Shuai, X.; Kasuya, K.-I.; Doi, Y.; Inoue, Y. Enzymatic degradation of atactic poly(R,S-3-hydroxybutyrate) induced by amorphous polymers and the enzymatic degradation temperature window of an amorphous polymer system. *Biomacromolecules* **2001**, *2*, 1045–1051. [CrossRef]

35. Liao, H.-T.; Wu, C.-S. Poly(3-hydroxybutyrate)/multi-walled carbon nanotubes nanocomposites: Preparation and characterizations. *Des. Monomers Polym.* **2013**, *16*, 99–107. [CrossRef]

36. Huh, M.; Jung, M.H.; Park, Y.S.; Kim, B.-J.; Kang, M.S.; Holden, P.J.; Yun, S.I. Effect of carbon nanotube functionalization on the structure and properties of poly(3-hydroxybutyrate)/MWCNTs biocomposites. *Macromol. Res.* **2014**, *22*, 765–772. [CrossRef]

37. Lim, S.T.; Hyun, Y.H.; Lee, C.H.; Choi, H.J. Preparation and characterization of microbial biodegradable poly(3-hydroxybutyrate)/ organoclay nanocomposite. *J. Mater. Sci. Lett.* **2003**, *22*, 299–302. [CrossRef]

38. Sanchez-Garcia, M.; Gimenez, E.; Lagaron, J. Morphology and barrier properties of nanobiocomposites of poly(3-hydroxybutyrate) and layered silicates. *J. Appl. Polym. Sci.* **2008**, *108*, 2787–2801. [CrossRef]

39. Bordes, P.; Pollet, E.; Bourbigot, S.; Averous, L. Structure and Properties of PHA/Clay Nano-Biocomposites Prepared by Melt Intercalation. *Macromol. Chem. Phys.* **2008**, *209*, 1473–1484. [CrossRef]

40. Eren, O.; Ucar, N.; Onen, A.; Karacan, I.; Kızıldag, N.; Demirsoy, N.; Vurur, O.F.; Borazan, I. Effect of differently functionalized carbon nanotubes on the properties of composite nanofibres. *Indian J. Fibre Text.* **2016**, *41*, 138–144.

41. Negahdary, M.; Behjati-Ardakani, M.; Heli, H. An electrochemical troponin T aptasensor based on the use of a macroporous gold nanostructure. *Microchim. Acta* **2019**, *186*, 377. [CrossRef]

42. Yu, H.-Y.; Qin, Z.-Y.; Sun, B.; Yang, X.-G.; Yao, J.-M. Reinforcement of transparent poly(3-hydroxybutyrate-co-3-hydroxyvalerate) by incorporation of functionalized carbon nanotubes as a novel bionanocomposite for food packaging. *Compos. Sci. Technol.* **2014**, *94*, 96–104. [CrossRef]

43. Lotti, N.; Pizzoli, M.; Ceccorulli, G.; Scandola, M. Binary blends of microbial poly(3-hydroxybutyrate) with polymethacrylates. *Polymer* **1993**, *34*, 4935–4940. [CrossRef]

44. Peng, H.; Alemany, L.B.; Margrave, J.L.; Khabashesku, V.N. Sidewall carboxylic acid functionalization of single-walled carbon nanotubes. *J. Am. Chem. Soc.* **2003**, *125*, 15174–15182. [CrossRef] [PubMed]

45. Du, F.; Wu, K.; Yang, Y.; Liu, L.; Gan, T.; Xie, X. Synthesis and electrochemical probing of water-soluble poly(sodium 4-styrenesulfonate-co-acrylic acid)-grafted multiwalled carbon nanotubes. *Nanotechnology* **2008**, *19*, 085716. [CrossRef] [PubMed]

46. Zhao, Z.; Yang, Z.; Hu, Y.; Li, J.; Fan, X. Multiple functionalization of multi-walled carbon nanotubes with carboxyl and amino groups. *Appl. Surf. Sci.* **2013**, *276*, 476–481. [CrossRef]

47. Singh, B.P.; Choudhary, V.; Teotia, S.; Gupta, T.K.; Nand, V.; Singh, S.R.D.; Mathur, R.B. Solvent free, efficient, industrially viable, fast dispersion process based amine modified MWCNT reinforced epoxy composites of superior mechanical properties. *Adv. Mater. Lett.* **2015**, *6*, 104–113. [CrossRef]

48. Schreiber, K.C. Infrared spectra of sulfones and related compounds. *Anal. Chem.* **1949**, *21*, 1168–1172. [CrossRef]

49. Amirian, M.; Chakoli, A.N.; Cai, W.; Sui, J. Effect of functionalized multiwalled carbon nanotubes on thermal stability of poly (L-LACTIDE) biodegradable polymer. *Sci. Iran.* **2013**, *20*, 1023–1027.

50. Mathur, R.; Pande, S.; Singh, B. Properties of PMMA/carbon nanotubes nanocomposites. *Polym. Nanotub. Nanocomposites Synth. Prop. Appl.* **2010**, *11*, 177.

51. Thakre, P.R.; Bisrat, Y.; Lagoudas, D.C. Electrical and mechanical properties of carbon nanotube-epoxy nanocomposites. *J. Appl. Polym. Sci.* **2010**, *116*, 191–202. [CrossRef]

52. Weber, M.; Kamal, M.R. Estimation of the volume resistivity of electrically conductive composites. *Polym. Compos.* **1997**, *18*, 711–725. [CrossRef]

53. Sandler, J.; Shaffer, M.; Prasse, T.; Bauhofer, W.; Schulte, K.; Windle, A. Development of a dispersion process for carbon nanotubes in an epoxy matrix and the resulting electrical properties. *Polymer* **1999**, *40*, 5967–5971. [CrossRef]

54. Song, S.; Xia, S.; Jiang, S.; Lv, X.; Sun, S.; Li, Q. A facile strategy to enhance the dielectric and mechanical properties of MWCNTs/PVDF composites with the aid of MMA-co-GMA copolymer. *Materials* **2018**, *11*, 347. [CrossRef]

55. Menon, A.V.; Madras, G.; Bose, S. Phase specific dispersion of functional nanoparticles in soft nanocomposites resulting in enhanced electromagnetic screening ability dominated by absorption. *Phys. Chem. Chem. Phys.* **2017**, *19*, 467–479. [CrossRef] [PubMed]

56. Pawar, S.; Shinde, K.; Bhosale, A.; Pawar, S. Studies on electric and dielectric properties of porous $Sm_{0.5}Sr_{0.5}CoO_{3-\delta}$. *J. Mater.* **2013**, *2013*, 987328. [CrossRef]

57. Zaki, H. AC conductivity and frequency dependence of the dielectric properties for copper doped magnetite. *Phys. B Condens. Matter* **2005**, *363*, 232–244. [CrossRef]

58. Lazarenko, A.; Vovchenko, L.; Prylutskyy, Y.; Matzuy, L.; Ritter, U.; Scharff, P. Mechanism of thermal and electrical conductivity in polymer-nanocarbon composites. *Mater. Werkst. Entwickl. Fert. Prüfung Eig. Anwend. Tech. Werkst.* **2009**, *40*, 268–272. [CrossRef]

59. Nayak, S.; Sahoo, B.; Chaki, T.K.; Khastgir, D. Development of polyurethane–titania nanocomposites as dielectric and piezoelectric material. *RSC Adv.* **2013**, *3*, 2620–2631. [CrossRef]

60. Alhusaiki-Alghamdi, H. Thermal and electrical properties of graphene incorporated into polyvinylidene fluoride/polymethyl methacrylate nanocomposites. *Polym. Compos.* **2017**, *38*, E246–E253. [CrossRef]

61. Chu, L.; Xue, Q.; Sun, J.; Xia, F.; Xing, W.; Xia, D.; Dong, M. Porous graphene sandwich/poly (vinylidene fluoride) composites with high dielectric properties. *Compos. Sci. Technol.* **2013**, *86*, 70–75. [CrossRef]

62. Garcia, O.P.; De Albuquerque, M.C.C.; Aquino, K.A.D.S.; Araujo, P.; Araujo, E. Use of lead (II) sulfide nanoparticles as stabilizer for PMMA exposed to gamma irradiation. *Mater. Res.* **2015**, *18*, 365–372. [CrossRef]

63. Huskić, M.; Žigon, M. PMMA/MMT nanocomposites prepared by one-step in situ intercalative solution polymerization. *Eur. Polym. J.* **2007**, *43*, 4891–4897. [CrossRef]

64. Meneghetti, P.; Qutubuddin, S. Synthesis of poly (methyl methacrylate) nanocomposites via emulsion polymerization using a zwitterionic surfactant. *Langmuir* **2004**, *20*, 3424–3430. [CrossRef] [PubMed]

65. Kashiwagi, T.; Inaba, A.; Brown, J.E.; Hatada, K.; Kitayama, T.; Masuda, E. Effects of weak linkages on the thermal and oxidative degradation of poly (methyl methacrylates). *Macromolecules* **1986**, *19*, 2160–2168. [CrossRef]

66. Demir, M.M.; Memesa, M.; Castignolles, P.; Wegner, G. PMMA/zinc oxide nanocomposites prepared by in-situ bulk polymerization. *Macromol. Rapid Commun.* **2006**, *27*, 763–770. [CrossRef]

67. Mathur, R.; Pande, S.; Singh, B.; Dhami, T. Electrical and mechanical properties of multi-walled carbon nanotubes reinforced PMMA and PS composites. *Polym. Compos.* **2008**, *29*, 717–727. [CrossRef]

68. Ishaq, M.; Saeed, K.; Shakirullah, M.; Ahmad, I.; Rehman, T. Effect of Coal Ash on the Morphological, Thermal and Mechanical Properties of Poly(methyl methacrylate). *J. Chil. Chem. Soc.* **2012**, *57*, 992–994. [CrossRef]

69. Kandare, E.; Deng, H.; Wang, D.; Hossenlopp, J.M. Thermal stability and degradation kinetics of poly(methyl methacrylate)/layered copper hydroxy methacrylate composites. *Polym. Adv. Technol.* **2006**, *17*, 312–319. [CrossRef]

70. Advincula, R.; University of Houston System. Polymer Nanocomposite Precursors with Carbon Nanotubes And/or Graphene and Related Thin Films and Patterning. U.S. Patent 8,932,671, 13 January 2015.

71. Madhukar, K.; Sainath, A.V.S.; Bikshamaiah, N.; Srinivas, Y.; Babu, N.M.; Ashok, B.; Kumar, D.S.; Rao, B.S. Thermal properties of single walled carbon nanotubes composites of polyamide 6/poly(methyl methacrylate) blend system. *J. Therm. Anal. Calorim.* **2014**, *115*, 345–354. [CrossRef]

72. Zhijiang, C.; Cong, Z.; Ping, X.; Jie, G.; Kongyin, Z. Calcium alginate-coated electrospun polyhydroxybutyrate/carbon nanotubes composite nanofibers as nanofiltration membrane for dye removal. *J. Mater. Sci.* **2018**, *53*, 14801–14820. [CrossRef]

73. Ndiaye, A.L.; Varenne, C.; Bonnet, P.; Petit, E.; Spinelle, L.; Brunet, J.; Pauly, A.; Lauron, B. Elaboration of single wall carbon nanotubes-based gas sensors: Evaluating the bundling effect on the sensor performance. *Thin Solid Film* **2012**, *520*, 4465–4469. [CrossRef]

74. Abraham, J.K.; Philip, B.; Witchurch, A.; Varadan, V.K.; Reddy, C.C. A compact wireless gas sensor using a carbon nanotube/PMMA thin film chemiresistor. *Smart Mater. Struct.* **2004**, *13*, 1045. [CrossRef]

75. Freeman, D.D.; Choi, K.; Yu, C. N-type thermoelectric performance of functionalized carbon nanotube-filled polymer composites. *PLoS ONE* **2012**, *7*, e47822. [CrossRef] [PubMed]

76. Aulenta, F.; Fuoco, M.; Canosa, A.; Petrangeli Papini, M.; Majone, M. Use of poly-β-hydroxy-butyrate as a slow-release electron donor for the microbial reductive dechlorination of TCE. *Water Sci. Technol.* **2008**, *57*, 921–925. [CrossRef] [PubMed]

77. Vaseashta, A.; Khudaverdyan, S. *Advanced Sensors for Safety and Security*; Springer: Berlin, Germany, 2013.

78. Assen, A.H.; Yassine, O.; Shekhah, O.; Eddaoudi, M.; Salama, K.N. MOFs for the sensitive detection of ammonia: Deployment of fcu-MOF thin films as effective chemical capacitive sensors. *ACS Sens.* **2017**, *2*, 1294–1301. [CrossRef]

79. Garg, N.; Kumar, M.; Kumari, N.; Deep, A.; Sharma, A.L. Chemoresistive Room-Temperature Sensing of Ammonia Using Zeolite Imidazole Framework and Reduced Graphene Oxide (ZIF-67/rGO) Composite. *ACS Omega* **2020**, *5*, 27492–27501. [CrossRef] [PubMed]

80. Ali, S.S.; Pauly, A.; Brunet, J.; Varenne, C.; Ndiaye, A.L. MWCNTs/PMMA/PS composites functionalized PANI: Electrical characterization and sensing performance for ammonia detection in a humid environment. *Sens. Actuators B Chem.* **2020**, *320*, 128364.

81. Maity, D.; Kumar, R.T.R. Polyaniline anchored MWCNTs on fabric for high performance wearable ammonia sensor. *ACS Sens.* **2018**, *3*, 1822–1830. [CrossRef]

82. Eising, M.; Cava, C.E.; Salvatierra, R.V.; Zarbin, A.J.G.; Roman, L.S. Doping effect on self-assembled films of polyaniline and carbon nanotube applied as ammonia gas sensor. *Sens. Actuators B Chem.* **2017**, *245*, 25–33. [CrossRef]

83. Ahmad, N.; Kausar, A.; Muhammad, B. An investigation on 4-aminobenzoic acid modified polyvinyl chloride/graphene oxide and PVC/graphene oxide based nanocomposite membranes. *J. Plast. Film Sheeting* **2016**, *32*, 419–448. [CrossRef]